sustainable chemistry

MDPI

Article

Valorization of Bio-Derived Calcium Carbonate from Asian Green Mussel Shell Waste in Hydrophobic Coatings for Reducing Pesticide Deposition on Mandarin Orange Surfaces

Sakunta Manakla [1], Sittinon Kerdtham [2], Susita Jinda [2], Chutiparn Lertvachirapaiboon [3], Sanong Ekgasit [4] and Tewarak Parnklang [2,*]

[1] Department of Nutrition and Dietetics, Faculty of Science and Technology, Valaya Alongkorn Rajabhat University Under the Royal Patronage, Khlong Nueng 13180, Thailand; sakunta@vru.ac.th
[2] Department of Industrial Chemistry, Faculty of Applied Science, King Mongkut's University of Technology North Bangkok, Bangkok 10800, Thailand; skerdtham@gmail.com (S.K.); susitajinda@gmail.com (S.J.)
[3] National Nanotechnology Center, National Science and Technology Development Agency, Khlong Luang 12120, Thailand; chutiparn.ler@nanotec.or.th
[4] Sensor Research Unit (SRU), Department of Chemistry, Faculty of Science, Chulalongkorn University, Bangkok 10330, Thailand; sanong.e@chula.ac.th
* Correspondence: tewarak.p@sci.kmutnb.ac.th

Abstract

This study developed an oleic acid (OA)-functionalized, bio-derived calcium carbonate (Bio-$CaCO_3$) filler recovered from Asian green mussel (*Perna viridis*) shell waste for incorporation into a hydroxypropyl methylcellulose (HPMC)-glycerol (Gro) matrix as a hydrophobic composite coating for reducing pesticide deposition on mandarin surfaces. Aragonite-rich Bio-$CaCO_3$ was extracted through a combined chemical treatment and mechanical pulverization process. The extracted Bio-$CaCO_3$ was characterized by scanning electron microscopy, X-ray diffraction, laser diffraction, and ATR FT-IR spectroscopy. At the optimal OA concentration, surface functionalization yielded OA-functionalized Bio-$CaCO_3$ (OA-Bio-$CaCO_3$) powder beds that exhibited apparent superhydrophobicity; successful functionalization was confirmed by X-ray photoelectron spectroscopy. The resulting HPMC-Gro-OA-Bio-$CaCO_3$ coating dispersion (CD-OA) formed hydrophobic composite films (f-CD-OA), as demonstrated by water contact-angle measurements and surface-morphology analysis. The CD-OA coating formulation was successfully applied to mandarin surfaces by a dip-coating process. Colorimetric screening indicated that organophosphate pesticide residues on coated mandarins did not exceed hazardous levels, even at 20 times the manufacturer-recommended application rate. Quantitative LC-MS/MS and GC-MS/MS analyses demonstrated that the optimized CD-OA coating formulation provided substantial short-term protection against acetamiprid and chlorothalonil with pesticide-deposition reductions of 89% and $\geq$96%, respectively, after 1 d relative to pristine mandarins. These findings advance the functional reuse of biogenic $CaCO_3$ and offer a simple, water-based dip-coating approach that provides temporary surface protection for citrus production and food-safety management.

Keywords: Asian green mussel shells; calcium carbonate; aragonite; pesticide deposition; mandarin oranges

Check for updates

Academic Editor: Konstantinos S. Triantafyllidis

Received: 8 June 2026
Revised: 14 August 2026
Accepted: 27 August 2026
Published: 8 September 2026

Copyright: © 2026 by the authors. Licensee MDPI, Basel, Switzerland. This article is an open access article distributed under the terms and conditions of the Creative Commons Attribution (CC BY) license.

1. Introduction

Mandarin orange (*Citrus reticulata*) is an economically important fruit crop belonging to the genus *Citrus* within the family *Rutaceae* [1,2]. Owing to its easy-to-peel rind, juicy texture, and desirable palatability, Mandarin orange is widely consumed worldwide as a fresh fruit [3]. Additionally, it is extensively utilized in the food industry for the production of juices, marmalades, jellies, candies, and flavoring agents [4,5]. Furthermore, mandarin peel by-products from industrial processing can be upcycled and processed into value-added products, including functional food preservatives [6], biodegradable active packaging [7], and nutraceuticals [8]. Mandarin orange is a source of vitamins, particularly vitamin C and vitamin A; essential macrominerals, including potassium, calcium, and phosphorus; flavonoids, such as hesperidin, naringin, nobiletin, tangeretin, and polymethoxylated flavones; phenolic acids; limonoids; and limonene [2,3]. The reported therapeutic properties of mandarin oranges, including antioxidant, anti-inflammatory, anticancer, antihypertensive, antimicrobial, and cardiovascular protective effects, may be attributed to these associated phytochemicals [5]. Moreover, the dried or aged peel of *Citrus reticulata*, commercially known as "Chenpi", has long been valued in traditional Chinese medicine and culinary applications because of its high concentration of bioactive compounds and distinctive flavor profile [9].

Mandarin production is threatened by insect pests, including the Asian citrus psyllid (*Diaphorina citri*), citrus whitefly (*Dialeurodes citri*), and other sap-sucking insects, as well as diseases such as huanglongbing (HLB) or citrus greening, sooty mold caused by *Capnodium citri*, dieback disease caused by *Colletotrichum gloeosporioides*, and witches' broom [10–13]. Effective management of these agricultural threats is essential for maintaining fruit quality and marketability and ensuring the economic sustainability of mandarin and citrus production. Mandarin oranges are exposed to multiple pesticide treatments during preharvest cultivation and postharvest handling to control insect pests, acarids, and fungal diseases [14,15]. Consequently, pesticide residues are frequently detected in mandarin oranges and other citrus fruits [16–18]. Because of the relatively short production cycle of citrus fruits, pesticides may be applied repeatedly from pre-flowering through fruit development and maturation [14]. In addition, mandarin oranges and other citrus fruits are commonly treated with postharvest fungicides, such as imazalil and thiabendazole, to suppress fungal spoilage and extend the fruit's shelf life during storage and transportation [19,20]. Residue levels, particularly those exceeding maximum residue limits (MRLs), may also result from non-compliance with good agricultural practices (GAP), including failure to observe preharvest intervals, excessive application rates, inappropriate application timing, and the use of unauthorized pesticide formulations [21,22]. Apart from direct application, pesticides can be introduced to mandarin orchards through environmental pathways, including contaminated irrigation water, soil containing persistent organic pollutants, and spray drift from adjacent treated agricultural fields [21,23]. The retention of pesticide residues is governed by the physicochemical properties of both the mandarin fruit surface and the pesticide formulation [15]. Non-systemic contact pesticides, such as chlorpyrifos, malathion, and cypermethrin, are lipophilic and often exhibit strong affinity for the waxy, lipid-rich outer peel of citrus fruit, hindering their removal by washing [19,22,24]. On the other hand, systemic pesticides, such as acetamiprid and imidacloprid, are sufficiently water-soluble to penetrate the fruit and translocate into the internal flesh, where their residues may persist [24,25]. Exposure to pesticide residues on mandarins and other citrus fruits may pose various health risks, particularly to children [20]. The co-occurrence of multiple pesticide residues may further increase toxicity through additive or synergistic effects [18]. Acute exposure can cause symptoms such as nausea, diarrhea, asthma, sore throat, dermatitis, and eye or skin irritation [19,26]. Chronic exposure to pesticide residues

has been associated with more serious health issues, including cancers, endocrine disruption, reproductive disorders, diabetes, neurodevelopmental impairments, and neurological diseases such as Parkinson's disease [15,18,19,26].

Practical strategies have been proposed to mitigate excessive exposure to pesticide residues on mandarins and citrus fruits. Reported preharvest approaches for reducing pesticide residues include integrated pest management [27], pesticide nanocapsules, and encapsulated nanopesticide formulations [28,29]. Peeling [19], non-toxic chemical washing using alkaline solutions [25] and electrolyzed water [30], ultrasound-assisted cleaning [31], and cold plasma technology [32] can also effectively reduce pesticide residue levels in postharvest fruits. Although edible and protective coatings have been extensively investigated for preserving the postharvest quality of mandarins [33–36], their potential to limit pesticide deposition and subsequent residue accumulation on fruits remains insufficiently explored. Because pesticide residues frequently accumulate on citrus peels, applying a protective coating to the fruit surface may offer a practical means of reducing residue accumulation while permitting continued crop-protection practices and potentially limiting consumer exposure [22]. Additionally, previous studies have predominantly focused on removing pesticide residues from fresh produce after contamination rather than preventing pesticide deposition using pre-applied coatings. For example, Cu^{2+}-chelated chitosan nanocrystals removed 80% of chlorpyrifos from contaminated strawberries after 1 min of washing and more than 98% after 2 min [37]. Similarly, metal–phenolic-network-capped starch nanoparticles removed more than 86% of thiabendazole, 93.51% of acetamiprid, and 89.03% of imidacloprid from contaminated apples [38]. A composite coating comprising guar gum, vinegar, and tamarind pulp was also reported to reduce chlorpyrifos residues, although the percentage reduction was not specified [39].

This study aimed to develop a hydrophobic composite film composed of cellulose-derived materials and Bio-$CaCO_3$ extracted from Asian green mussel (*Perna viridis*) shell waste to minimize pesticide deposition on mandarin fruit surfaces during pesticide application. Hydroxypropyl methylcellulose (HPMC) serves both as the film-forming matrix and a dispersing/stabilizing agent to promote homogeneous distribution of $CaCO_3$ within the composite. HPMC has been widely investigated as a film-forming matrix in edible coatings for fresh produce, including fruits and vegetables [40–42]. $CaCO_3$ is also well-suited for plant-surface coating applications because it is not classified as a carcinogen, has not been associated with reproductive toxicity in humans, can degrade into compounds that supply beneficial nutrients to plants, and does not persist or accumulate in the environment [43]. Previous field research demonstrated the feasibility of using $CaCO_3$ as a reflective foliar coating in citrus production. Monthly applications of $CaCO_3$ to the canopies of 'Navelina ISA 315' sweet orange trees [*Citrus sinensis* (L.) Osbeck] during summer mitigated heat and radiation stress, thereby improving photosynthetic performance, light penetration, fruit quality, peel coloration, and yield [44]. Preharvest application of $CaCO_3$ nanoparticles onto pineapple fruit could reduce sunburn damage and enhance fruit quality [45]. Particle films of $CaCO_3$ have been demonstrated to provide artificial shading and photoprotective effects in American grapevines (*Vitis labrusca* L.) [46], tomato plants [47], and conilon coffee trees [48].

Green mussel shells were selected as a renewable and cost-effective source for biogenic $CaCO_3$ because they are primarily composed of 95% to 99% carbonate-bearing minerals with only a small fraction (1% to 5%) of organic matter [49]. The valorization of Asian green mussel shell waste also offers several environmental benefits, including reducing the burden on landfills and the associated pollution [50], lowering greenhouse gas emissions relative to limestone mining [51], and supporting circular economy principles [52]. Additionally, $CaCO_3$ polymorphs in *Perna viridis* shells have been reported

to occur exclusively as aragonite [53], offering numerous advantages, including excellent biocompatibility and reliable processing into $CaCO_3$-based biomaterials [54,55]. Previous studies have employed concentrated alkaline treatments to deproteinize mussel shells and remove organic constituents, including silk-fibroin-like proteins, β-chitin, glycoproteins, and the outer periostracum layer [56–59]. Such treatments may preserve the structural integrity of the nacreous layer, which comprises alternating layers of organic matrix and aragonitic calcium carbonate interconnected by mineral bridges, although removal of the organic material may leave air gaps within the structure [60]. Aragonite $CaCO_3$ microparticles extracted from Asian green mussel shells exhibited bioinsecticide activity against mealybugs [61]. Additionally, mussel-shell mulch was employed as an optical barrier that altered the flying/hovering and landing behavior of a melolonthine pest, resulting in a 46% reduction in vineyard damage and a 28% enhancement in grape yield [62]. Aragonite $CaCO_3$ derived from green mussel shells can be chemically surface-modified with fatty acids to impart hydrophobic properties [63]. In this study, oleic acid (OA) was selected as a surface-modifying agent to impart hydrophobicity to inherently hydrophilic $CaCO_3$ [64]. Oleic acid-functionalized $CaCO_3$ could reduce agglomeration and improve suspension stability in water, which is beneficial for aqueous-based coating dispersions [65].

Incorporating oleic acid-functionalized Bio-$CaCO_3$ (OA-Bio-$CaCO_3$) recovered from Asian green mussel shells into an HPMC-glycerol composite coating formulation may provide an effective strategy for reducing pesticide deposition on mandarin surfaces. Three pesticide treatments were evaluated: a combined cypermethrin-profenofos formulation, acetamiprid, and chlorothalonil. Cypermethrin and profenofos are non-systemic broad-spectrum insecticides. Cypermethrin is a type II synthetic pyrethroid and an Insecticide Resistance Action Committee (IRAC) Group 3A sodium-channel modulator, whereas profenofos is an organophosphate insecticide and acaricide classified as an IRAC Group 1B acetylcholinesterase inhibitor [66–68]. Acetamiprid is a systemic neonicotinoid insecticide classified by the Insecticide Resistance Action Committee as a Group 4A nicotinic acetylcholine receptor (nAChR) competitive modulator [68,69]. Chlorothalonil is a broad-spectrum, non-systemic chloronitrile fungicide classified by the Fungicide Resistance Action Committee as an M05 multisite fungicide [70,71]. Acetamiprid is substantially more polar and hydrophilic than chlorothalonil, as indicated by its lower octanol–water partition coefficient (log K_{ow}; 0.80 versus 2.94 at pH 7 and 20 °C) and markedly higher water solubility (2950 mg L^{-1} at 20 °C versus 0.81 mg L^{-1} at 25 °C) [72–74]. Conversely, chlorothalonil is relatively lipophilic and exhibits greater affinity for hydrophobic phases [75]. The cypermethrin-profenofos formulation was employed for preliminary screening of pesticide-deposition reduction on mandarins using an available colorimetric test kit. Acetamiprid and chlorothalonil were subsequently selected as representative pesticides with contrasting physicochemical properties and systemic behaviors to quantitatively evaluate the efficacy of the developed HPMC-glycerol-OA-Bio-$CaCO_3$ composite coating in reducing pesticide deposition on mandarin surfaces.

2. Experimental Section

2.1. Materials and Chemicals

The green mussel (*Perna viridis*) shells utilized in this study were sourced from the Laem Yai community in Samut Songkhram Province, Thailand. An aqueous hydrogen peroxide solution (50.1–50.8%) and potassium hydroxide pellets (KOH, 90%) were obtained from Krungthepchemi Co., Ltd. (Bangkok, Thailand). Glycerol (99.5%) and hydroxypropyl methylcellulose (HPMC, 50 cP at 2% (*w*/*w*)) were acquired from Chanjao Longevity Co., Ltd. (Bangkok, Thailand). Commercial pesticide formulations, including cypermethrin + profenofos (4% + 40% (*w*/*v*), emulsifiable concentrate (EC)), acetamiprid (20% (*w*/*v*),

soluble concentrate (SL)), and chlorothalonil (50% (*w*/*v*), suspension concentrate (SC)), were purchased from NC Agrochem Co., Ltd. (Nakhon Nayok, Thailand), Apple agro 89 (Nakhon Pathom, Thailand), and Yakest.online (Phra Nakhon Si Ayutthaya, Thailand), respectively, and used as model pesticides. Sodium carbonate (E 500) was procured from SML Chemrich Co., Ltd. (Bangkok, Thailand). Mandarin oranges (*Citrus reticulata*) were obtained from a local market in Nonthaburi, Thailand. Oleic acid (*cis*-9-octadecenoic acid) (technical grade, 90%) was purchased from Sigma-Aldrich Co., LLC. (St. Louis, MO, USA). All chemicals were used as received without further purification. Ultrapure water (18.2 MΩ·cm) was produced by a Sartorius arium® pro water system (Sartorius Lab Instruments GmbH & Co. KG, Goettingen, Germany).

2.2. Extraction of Bio-$CaCO_3$ from Waste Green Mussel Shells

The extraction procedure of bio-based calcium carbonate (Bio-$CaCO_3$) was adapted from previously reported methods [60,76] with some modifications. Green mussel shells were soaked in water for 1–3 d under ambient laboratory conditions (32.0 ± 1.0 °C and 62 ± 1% relative humidity) and then thoroughly washed to remove adhering particulate matter, including coarse sand and dust, as well as residual flesh, filaments, and water-soluble impurities. The cleaned shells were subsequently dried in sunlight and designated as cleaned green mussel shells (C-GMS). Subsequently, the C-GMS were immersed in a 1 M KOH solution for a minimum of 7 d to eliminate the organic shell matrix known as conchixes [77]. After alkali treatment, the shells were rinsed thoroughly with tap water until a neutral pH was achieved to ensure the complete removal of residual alkali. After cleaning and drying, the dried shells were thermally treated at 200 °C for 2 h in a BINDER FED 115 drying and heating chamber (BINDER GmbH, Tuttlingen, Germany). The treated shells were subsequently allowed to cool to room temperature before further processing. Following thermal treatment, the shells were immersed in water for 24 h to eliminate residual organic matrices. The shells were then thoroughly washed with tap water and dried under ambient conditions and designated as PT-GMS. The C-GMS and PT-GMS shells were separately pre-pulverized into processable powders using a Samyod SAM-3F electric grinder (Samyod Agricultural Machinery Co., Ltd., Ubon Ratchathani, Thailand) with a power rating of 3 HP and a rotating speed of 5500 rpm. The resulting pre-pulverized green mussel shell powders were designated C-GMS (RM) and Bio-$CaCO_3$ (RM), respectively. The Bio-$CaCO_3$ (RM) powder was bleached in a 50% (*w*/*w*) H_2O_2 solution for 3 h [56]. Subsequently, a 400 g batch of the H_2O_2-bleached Bio-$CaCO_3$ (RM) powder was further ground at 25,000 rpm for 30 s using a DFY-500C high-speed grinder (Wenling Linda Machinery Co., Ltd., Wenling, Zhejiang, China). The resulting fine, unsieved powder was designated Bio-$CaCO_3$ (NSif).

2.3. Surface Modification of Bio-$CaCO_3$ with Oleic Acid

Prior to surface functionalization, the extracted Bio-$CaCO_3$ (NSif) powder was passed through a 200-mesh sieve. The sieved Bio-$CaCO_3$ particles, designated as Bio-$CaCO_3$ (Sif), were subsequently functionalized with oleic acid (OA) to render their inherently hydrophilic surfaces hydrophobic [78]. Typically, 20 g of Bio-$CaCO_3$ (Sif) was transferred to a 250 mL beaker containing 45 mL of ultrapure water. The resulting suspension was heated to 75 °C under continuous stirring. OA was then added to achieve a final concentration of 1.0, 2.0, 3.0, 4.0, or 6.0% (*w*/*v*), and the mixture was stirred for an additional 30 min. Upon completion, the suspension was filtered to collect the solid residue. The recovered solids were dried in an air-circulated oven at 120 °C for 1 h to remove residual moisture [79]. The final oleic acid-functionalized Bio-$CaCO_3$ was designated as OA-Bio-$CaCO_3$. Unless otherwise stated, OA-Bio-$CaCO_3$ was prepared by modifying 20 g of Bio-$CaCO_3$ (Sif) with

OA at a concentration of 3.0% (*w*/*v*). Table 1 summarizes the sample codes used throughout the extraction and surface functionalization of Bio-$CaCO_3$.

Table 1. Sample nomenclature and corresponding processing procedures for bio-derived calcium carbonate (Bio-$CaCO_3$), including mechanical pulverization, bleaching, high-speed grinding, 200-mesh sieving, and surface functionalization with oleic acid (OA).

Sample Designation	Processing Procedures
C-GMS	Cleaned and dried green mussel shells
C-GMS (RM)	Mechanically pulverized C-GMS powder
PT-GMS	C-GMS subjected to sequential alkaline treatment, tap-water washing and drying, thermal treatment at 200 °C for 2 h, tap-water immersion, and final washing and drying
Bio-$CaCO_3$ (RM)	Mechanically pulverized PT-GMS powder
Bio-$CaCO_3$ (NSif)	Unsieved Bio-$CaCO_3$ powder produced by high-speed grinding of H_2O_2-bleached Bio-$CaCO_3$ (RM) powder
Bio-$CaCO_3$ (Sif)	Bio-$CaCO_3$ (NSif) powder passed through a 200-mesh sieve
OA-Bio-$CaCO_3$	Bio-$CaCO_3$ (Sif) particles surface-functionalized with OA

2.4. Preparation of Composite Coating Dispersions

An HPMC-glycerol (HPMC-Gro) mixture was prepared by mixing 5.0% (*w*/*v*) HPMC and 7.0% (*w*/*v*) Gro in 100 mL of ultrapure water under vigorous magnetic stirring at 60 °C. After cooling to room temperature, the mixture was further sonicated in an Elmasonic P60H ultrasonic cleaner (Elma Schmidbauer GmbH, Singen, Germany) to facilitate the solubilization of HPMC and Gro in the dispersing medium. The power output, frequency, and duration of the ultrasonication were 150 W, 37 kHz, and 10 min, respectively.

A coating dispersion was typically prepared by dispersing 10.0–25.0% (*w*/*v*) OA-Bio-$CaCO_3$ in 100 mL of the HPMC-glycerol mixture at 85 °C with continuous magnetic stirring for 10 min. After cooling to room temperature, the dispersion was degassed using a vacuum pump and subsequently ultrasonicated with a Sonics® VCX750 ultrasonic processor (Sonics & Materials, Inc., Newtown, CT, USA) at a frequency of 20 kHz. The sonication power was 500 W. The pulse-on and pulse-off intervals were equally set at 30 s, and the sonication duration was 5 min. After sonication, the hydrophobic coating dispersion was stored under ambient conditions for an additional 24 h prior to use. The compositions of the coating dispersions and their corresponding designations are summarized in Table 2.

Table 2. Compositions and sample codes of HPMC-Gro composite coating formulations containing different concentrations of OA-Bio-$CaCO_3$ or sieved, unmodified Bio-$CaCO_3$ [Bio-$CaCO_3$ (Sif)].

Coating Dispersion Designation	HPMC Concentration (% (*w*/*v*))	Glycerol (Gro) Concentration (% (*w*/*v*))	OA-Bio-$CaCO_3$ Concentration (% (*w*/*v*))	Bio-$CaCO_3$ (Sif) Concentration (% (*w*/*v*))
CD-BF0	5.0	7.0	0	0
CD-OA1	5.0	7.0	10.0	0
CD-OA2	5.0	7.0	15.0	0
CD-OA3	5.0	7.0	20.0	0
CD-UM3	5.0	7.0	0	20.0
CD-OA4	5.0	7.0	25.0	0

2.5. Preparation of Free-Standing Composite Films

Free-standing composite films were prepared by solution casting. Briefly, a 10.00 mL aliquot of each coating dispersion (CD-BF0, CD-OA1, CD-OA2, CD-OA3, CD-UM3, or CD-OA4) was cast into a separate Petri dish (15 mm height × 100 mm diameter) and dried in a desiccator for 24 h under laboratory ambient conditions (32.0 ± 1.0 °C and 62 ± 1% relative humidity). The film designations and corresponding film-forming dispersions are summarized in Table 3.

Table 3. Sample designations of solution-cast HPMC-glycerol (Gro) composite films from various starting coating dispersions.

Composite Film Designation	Corresponding Film-Forming Dispersion
f-CD-BF0	CD-BF0
f-CD-OA1	CD-OA1
f-CD-OA2	CD-OA2
f-CD-OA3	CD-OA3
f-CD-UM3	CD-UM3
f-CD-OA4	CD-OA4

The thickness of each free-standing composite film specimens was measured at five different positions using a digital micrometer (Mitutoyo (Thailand) Co., Ltd., Bangkok, Thailand) with a measurement range of 0−25 mm and a resolution of 0.001 mm. Values are reported as the mean ± standard deviation of three independent replicates (n = 3). The measured thicknesses of the f-CD-BF0, f-CD-OA1, f-CD-OA2, f-CD-OA3, f-CD-UM3, and f-CD-OA4 films were 137 ± 6, 254 ± 14, 259 ± 23, 269 ± 18, 269 ± 31, and 275 ± 26 μm, respectively.

2.6. Evaluation of Protection Against Pesticide Deposition

Mandarin orange samples were initially immersed in a 10% (w/v) aqueous sodium carbonate solution at 25 °C for 20 min, following a previously reported method [25]. The average fruit mass, determined from a subset of 24 mandarins, was 159.60 ± 19.58 g. The treated samples were then dried under ambient conditions (32.0 ± 1.0 °C and 62 ± 1% relative humidity) for 60 min, placed in sample bags, and stored at 4 °C for 24 h. Following storage, the samples were designated as P-ManOr.

Subsequently, the P-ManOr samples were immersion-coated in either the CD-OA3 or CD-UM3 coating dispersion for 30 s and dried under ambient conditions for an additional 2 h before pesticide application. Table 4 summarizes the mandarin orange samples and corresponding coating treatments used to evaluate protection against pesticide deposition. The measured coating thicknesses of the OA-ManOr and UM-ManOr samples were 48 ± 4 and 48 ± 6 μm, respectively. Values are reported as the mean ± standard deviation of three independent replicates (n = 3).

Table 4. Sample designations and corresponding coating treatments for uncoated control mandarin oranges and mandarin oranges coated with HPMC-glycerol formulations containing oleic acid-functionalized bio-derived calcium carbonate (OA-Bio-$CaCO_3$) or sieved, unmodified Bio-$CaCO_3$ [Bio-$CaCO_3$ (Sif)].

Mandarin Sample Designation	Coating Treatment
P-ManOr	None
OA-ManOr	CD-OA3 for 30 s + drying for 2 h
UM-ManOr	CD-UM3 for 30 s + drying for 2 h

In a preliminary screening study, P-ManOr, OA-ManOr, and UM-ManOr samples were sprayed with a commercial emulsifiable-concentrate formulation containing 4% (*w*/*v*) cypermethrin and 40% (*w*/*v*) profenofos. The formulation was diluted with ultrapure water at pesticide-to-water ratios of 3.0:100 (*v*/*v*) and 4.5:100 (*v*/*v*), corresponding to 20 and 30 times the label-recommended application ratio of 1.5:1000 (*v*/*v*), respectively. Approximately 5.00 mL of the diluted pesticide formulation was applied to each individual fruit. The samples were subsequently allowed to dry under ambient conditions for 1 h. Following spraying, the samples were stored at ambient temperature for an additional 24 h and subsequently screened for organophosphate pesticide residues using the "GT" Pesticide Test Kit (B Smart Science Co., Ltd., Nonthaburi, Thailand). Table 5 summarizes the sample designations and corresponding treatment conditions used to evaluate the efficacy of the coatings in reducing cypermethrin-profenofos deposition on mandarin surfaces.

Table 5. Sample designations and corresponding treatment conditions for mandarin orange samples exposed to the cypermethrin-profenofos formulation.

Sample Designation	Model Pesticide and Treatment Conditions
Prof20x_P-ManOr1	P-ManOr treated with a cypermethrin-profenofos formulation at a formulation-to-water ratio of 3.0:100 (*v*/*v*), dried for 1 h, and analyzed after 1 d
Prof30x_P-ManOr1	P-ManOr treated with a cypermethrin-profenofos formulation at a formulation-to-water ratio of 4.5:100 (*v*/*v*), dried for 1 h, and analyzed after 1 d
Prof20x_OA-ManOr1	OA-ManOr treated with a cypermethrin-profenofos formulation at a formulation-to-water ratio of 3.0:100 (*v*/*v*), dried for 1 h, and analyzed after 1 d
Prof30x_OA-ManOr1	OA-ManOr treated with a cypermethrin-profenofos formulation at a formulation-to-water ratio of 4.5:100 (*v*/*v*), dried for 1 h, and analyzed after 1 d
Prof20x_UM-ManOr1	UM-ManOr treated with a cypermethrin-profenofos formulation at a formulation-to-water ratio of 3.0:100 (*v*/*v*), dried for 1 h, and analyzed after 1 d
Prof30x_UM-ManOr1	UM-ManOr treated with a cypermethrin-profenofos formulation at a formulation-to-water ratio of 4.5:100 (*v*/*v*), dried for 1 h, and analyzed after 1 d

For a systematic evaluation of the CD-OA3 coating's ability to reduce pesticide deposition, P-ManOr and OA-ManOr samples were sprayed with either acetamiprid or chlorothalonil. The commercial acetamiprid formulation contained 20% active ingredient and was supplied as a soluble concentrate (20% SL), with a label-recommended application rate of 4 mL per 20 L of water. The commercial chlorothalonil formulation contained 50% active ingredient and was supplied as a suspension concentrate (50% SC), with a recommended application rate of 20 mL per 20 L of water. Acetamiprid and chlorothalonil spray solutions were prepared at eightfold and twofold their respective label-recommended application rates to simulate pesticide overapplication and ensure residue levels sufficient for quantitative analysis. Under Regulation (EC) No 396/2005, the maximum residue levels (MRLs) for acetamiprid and chlorothalonil in whole mandarins are 0.9 and 0.01 mg/kg, respectively, with the latter corresponding to the lower limit of analytical quantification [80,81]. Both pesticide formulations were diluted with ultrapure water to provide nominal acetamiprid and chlorothalonil application levels of approximately 10 and 30 mg/kg of whole mandarin fruit, respectively. Each treatment group comprised 500 g of mandarin fruit, and approximately 5.00 mL of the corresponding pesticide solution

was sprayed uniformly over the surface of each fruit. The treated fruits were dried under ambient conditions for 1 h and subsequently stored at ambient conditions for either 1 or 7 d before pesticide-residue analysis. Table 6 summarizes the sample designations and corresponding treatment conditions used to evaluate the efficacy of the CD-OA3 coating in reducing the deposition of acetamiprid and chlorothalonil on mandarin surfaces.

Table 6. Sample designations and corresponding treatment conditions for mandarin orange samples exposed to acetamiprid and chlorothalonil, with or without simulated rainfall treatment.

Sample Designation	Model Pesticide and Treatment Conditions
Acet_P-ManOr1	P-ManOr treated with acetamiprid at 10 mg/kg, dried for 1 h, and analyzed after 1 d
Acet_P-ManOr7	P-ManOr treated with acetamiprid at 10 mg/kg, dried for 1 h, and analyzed after 7 d
Acet_OA-ManOr1	OA-ManOr treated with acetamiprid at 10 mg/kg, dried for 1 h, and analyzed after 1 d
Acet_OA-ManOr7	OA-ManOr treated with acetamiprid at 10 mg/kg, dried for 1 h, and analyzed after 7 d
Acet_SR_OA-ManOr1	OA-ManOr exposed to simulated rainfall, dried for 1 h, treated with acetamiprid at 10 mg/kg, dried for 1 h, and analyzed after 1 d
Ctnl_P-ManOr1	P-ManOr treated with chlorothalonil at 30 mg/kg, dried for 1 h, and analyzed after 1 d
Ctnl_P-ManOr7	P-ManOr treated with chlorothalonil at 30 mg/kg, dried for 1 h, and analyzed after 7 d
Ctnl_OA-ManOr1	OA-ManOr treated with chlorothalonil at 30 mg/kg, dried for 1 h, and analyzed after 1 d
Ctnl_OA-ManOr7	OA-ManOr treated with chlorothalonil at 30 mg/kg, dried for 1 h, and analyzed after 7 d
Ctnl_SR_OA-ManOr1	OA-ManOr exposed to simulated rainfall, dried for 1 h, treated with chlorothalonil at 30 mg/kg, dried for 1 h, and analyzed after 1 d

The performance of the CD-OA3 coating under simulated rainfall was evaluated using approximately 500 g of OA-ManOr samples per treatment. A total of 610 mL of water was sprayed uniformly over a test area measuring 19.5 × 25.0 cm (487.5 cm^2) within 5 min, corresponding to a simulated rainfall depth of approximately 12.5 mm and an equivalent rainfall intensity of approximately 150 mm h^{-1}. According to the adopted rainfall-intensity classification, this treatment represents violent rainfall [82]. Following exposure to the simulated rainfall, the OA-ManOr samples were dried at room temperature for 1 h. Each fruit was subsequently sprayed with 5.00 mL of either the prepared acetamiprid or chlorothalonil solution and dried at room temperature for an additional 1 h. The samples were then collected and stored at ambient conditions for 1 d before pesticide-residue analysis.

2.7. Characterization

2.7.1. Field-Emission Scanning Electron Microscopy and Energy-Dispersive X-Ray Spectroscopy

The particle morphology of the extracted Bio-$CaCO_3$ specimen was investigated and compared with that of the C-GMS (RM) particles. The test specimen was prepared by dispersing 0.1 g of the specified powdered sample in 50 mL of ultrapure water. A 1 µL aliquot of the dispersion was then pipetted onto a glass slide, air-dried in a desiccator for

at least 24 h, and subsequently dried in an air-circulated oven at 60 °C for an additional 1 h. The dried powdered specimen was collected using carbon adhesive tape firmly affixed to an aluminum stub and thoroughly dried in an air-circulated oven at 60 °C for 30 min prior to analysis. All samples were examined using a Quanta^{TM} FEG 250 field-emission scanning electron microscope (FE-SEM) (FEI Company, part of Thermo Fisher Scientific, Hillsboro, OR, USA) operated at an accelerating voltage of 15.0 kV. Before micrograph acquisition, all samples were coated with a thin gold layer using a JEOL JFC-1200 ion sputtering device (JEOL Ltd., Tokyo, Japan). To determine the mean particle length of the extracted Bio-$CaCO_3$ (Sif) sample, individual particle lengths were also measured directly from FE-SEM micrographs using ImageJ software (version 1.54p), a Java-based image analysis program developed by the National Institute of Mental Health [83]. At least 300 particles from 10 different micrographs were examined.

The elemental compositions of the peel surfaces of P-ManOr, OA-ManOr, and OA-ManOr washed with ultrapure water (Washed OA-ManOr) were analyzed by energy-dispersive X-ray spectroscopy (EDS) using a Quanta 250 FEG analytical field-emission scanning electron microscope equipped with an INCAx-act EDS detector incorporating PentaFET Precision technology (Oxford Instruments Pte. Ltd., Singapore). The analyses were performed at an accelerating voltage of 15.00 kV.

2.7.2. X-Ray Diffraction

The crystal polymorphs of the C-GMS (RM) and Bio-$CaCO_3$ (Sif) samples were investigated by X-ray diffraction analysis. X-ray diffractograms were obtained using a Bruker AXS Model D8 Discover X-ray diffractometer (Bruker AXS GmbH, Karlsruhe, Germany) operating at 40 kV and 40 mA with Cu Kα radiation (λ = 1.54060 Å). The dried samples were scanned continuously over a 2θ range of 10 to 60°, with a step size of 0.0200°. The diffraction planes of the C-GMS (RM) and Bio-$CaCO_3$ (Sif) powders were indexed by comparing the experimental *d*-spacing values with those theoretically calculated for orthorhombic aragonite $CaCO_3$ crystals. The lattice parameters of orthorhombic aragonite $CaCO_3$ based on the JCPDS Database Card No. 05-0453 are a = 4.95900 Å, b = 7.96800 Å, and c = 5.74100 Å [84]. The lattice parameter equation for orthorhombic aragonite $CaCO_3$ is expressed in Equation (1) [85].

$$\left(\frac{1}{d_{hkl}}\right)^2 = \frac{h^2}{a^2} + \frac{k^2}{b^2} + \frac{l^2}{c^2} \quad (1)$$

Here, d_{hkl} is the interplanar spacing, h, k, and l are Miller indices, and a, b, and c are the orthorhombic lattice parameters.

2.7.3. Laser Diffraction

Laser diffraction particle size analysis was conducted to evaluate the particle statistics of the C-GMS (RM) and Bio-$CaCO_3$ (Sif) samples. Prior to analysis, each specimen was dispersed in deionized water to a final concentration of 0.01–2.5% (w/v) using a SONICS.com VCX750 ultrasonic processor (Sonics & Materials, Inc., Newtown, CT, USA) to ensure adequate dispersion. The prepared suspension was then introduced into a liquid cell of a Partica LA-960V2 laser scattering particle size distribution analyzer (HORIBA (Thailand) Limited, Bangkok, Thailand). Particle distribution characteristics, including span, specific surface area, the volumetric mean diameter (D[4,3]; De Brouckère mean diameter), and the surface-weighted mean diameter (D[3,2]; Sauter mean diameter), were determined from

the volume-based particle size distribution data [86,87]. $D[4,3]$ and $D[3,2]$ were determined using Equations (2) and (3), respectively [88]:

$$D[4,3] = \frac{\sum_{i=1}^{n} d_i^4}{\sum_{i=1}^{n} d_i^3} \quad (2)$$

$$D[3,2] = \frac{\sum_{i=1}^{n} d_i^3}{\sum_{i=1}^{n} d_i^2} \quad (3)$$

where d_i is the diameter of the i^{th} particle. For each sample, laser diffraction particle size measurements were performed using three independent replicates (n = 3). Values of $D[4,3]$, $D[3,2]$, span, and specific surface area are reported as the mean ± standard deviation.

2.7.4. ATR FT-IR Spectroscopy

Chemical functional groups on the surfaces of Bio-$CaCO_3$ (Sif), OA-Bio-$CaCO_3$, f-CD-BF0 films, and f-CD-OA3 films were characterized using ATR FT-IR spectroscopy. ATR FT-IR spectra were acquired using a Nicolet iS5 FT-IR spectrophotometer (Thermo Scientific, Waltham, MA, USA) equipped with a fast recovery deuterated triglycine sulfate (DTGS) detector. An iD5 single-bounce ATR accessory with a laminated-diamond crystal was employed as a sampling probe. To obtain an infrared spectrum, the dried specimen was placed onto a flat diamond crystal internal reflection element (IRE) with a sampling diameter of 1.5 mm. The specimen was pressed against the flat diamond crystal with a pressure device until the maximum allowable pressure was reached. All ATR FT-IR spectra were collected at a resolution of 4 cm^{-1}. Each spectrum was averaged over 32 co-added scans.

2.7.5. X-Ray Photoelectron Spectroscopy

The surface chemical compositions of Bio-$CaCO_3$ (Sif) and OA-Bio-$CaCO_3$ were analyzed using X-ray photoelectron spectroscopy. XPS spectra were obtained using a PHI VersaProbe 4 X-ray photoelectron spectrometer (Physical Electronics, Inc., Chanhassen, MN, USA) equipped with a monochromatized Al K_α X-ray source with a photon energy of 1486.6 eV, operated at 25.0 W. Charge neutralization was applied at 1.0 V and 3.0 μA. The analyzer was operated in fixed analyzer transmission (FAT) mode. Survey spectra were acquired over a binding-energy range of 1450 to −1 eV using a pass energy of 224.0 eV, an energy step size of 0.80 eV, and a dwell time of 0.200 s per data point. The binding energies of the high-resolution spectra were calibrated against the aliphatic C–C/C–H component of the C 1s peak at 285.0 eV. High-resolution spectra were collected for the C 1s, O 1s, and Ca 2p regions using a pass energy of 69.0 eV, an energy step size of 0.13 eV, and a dwell time of 0.800 s per data point. The binding-energy ranges were 362–338 eV for Ca 2p, 306–268 eV for C 1s, and 547–523 eV for O 1s.

2.7.6. Water Contact Angle Measurements

The wettability of Bio-$CaCO_3$ (Sif) and OA-Bio-$CaCO_3$ powders and the f-CD-BF0, f-CD-OA1, f-CD-OA2, f-CD-OA3, f-CD-UM3, and f-CD-OA4 composite films was evaluated by static water contact angle (WCA) measurements using an OCA 15plus contact angle meter (DataPhysics Instruments GmbH, Filderstadt, Germany). For powder analysis, 0.5 g of Bio-$CaCO_3$ (Sif) or OA-Bio-$CaCO_3$ was placed on a glass microscope slide and gently compressed using a cover glass to produce a macroscopically flat, compact, and crack-free

powder bed. The composite films were cut into rectangular specimens measuring 2 × 7 cm. Measurements were conducted at 25 °C and 60 ± 2% relative humidity using the sessile-drop method. A 9.0 µL droplet of deionized water was deposited onto the sample surface, and an image was acquired 5 s after droplet deposition. This time point was defined as the initial measurement (nominally 0 min). For each sample, contact-angle measurements were performed using three independent replicates (n = 3) and analyzed using SCA 20 software (version 4.4.1, build 1046) (DataPhysics Instruments GmbH). The results are reported as the mean ± standard deviation. For the compressed powder beds, the measured values represent apparent contact angles because surface roughness, interparticle porosity, packing density, and liquid penetration can influence droplet behavior [89]. Accordingly, these measurements were used for comparative evaluation of the wettability of Bio-$CaCO_3$ (Sif) and OA-Bio-$CaCO_3$ prepared and measured under identical conditions, rather than for determining their intrinsic equilibrium contact angles.

2.7.7. Digital Photography

Photographic images of the specimens were acquired using a Panasonic Lumix G100 digital camera (Panasonic (Thailand) Co., Ltd., Samut Prakan, Thailand) at a resolution of 20.3 megapixels.

2.7.8. Rapid Screening of Organophosphate Pesticide Residues

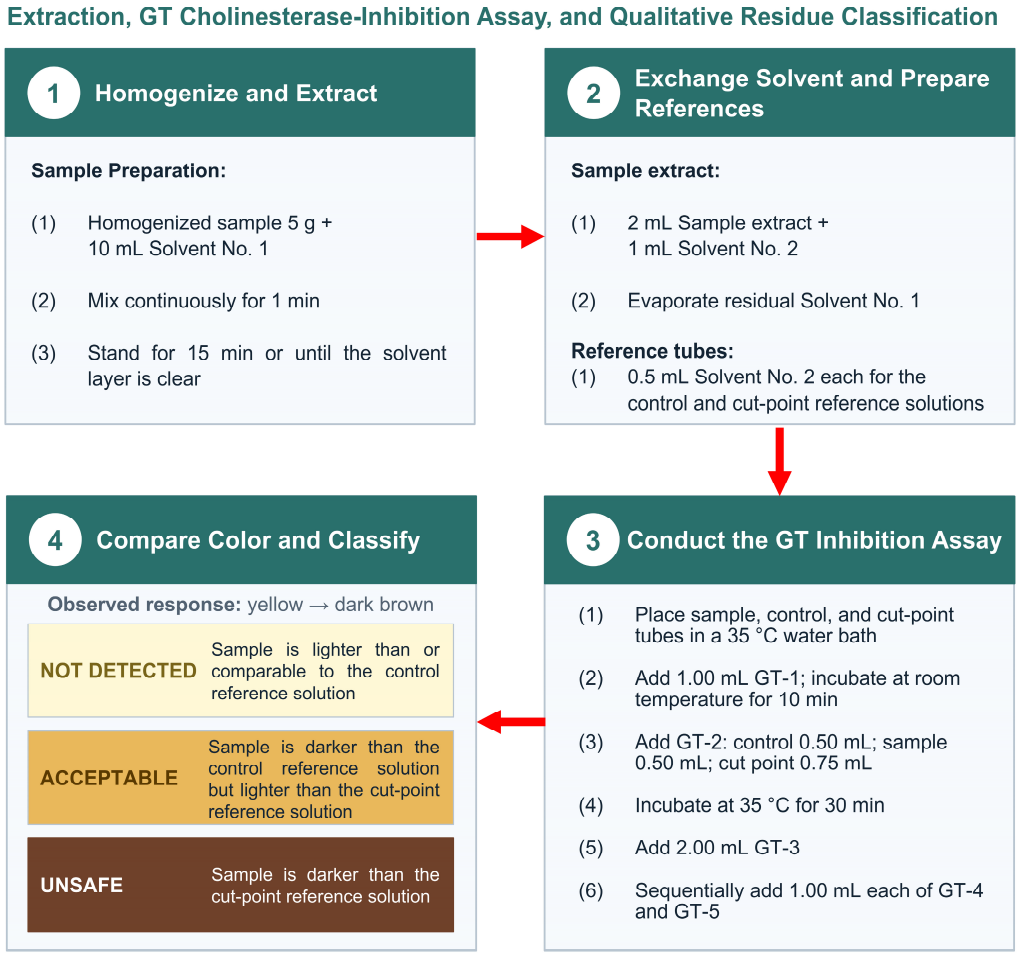
The "GT" Pesticide Test Kit is intended for the rapid and field-deployable screening of organophosphate and carbamate pesticide residues, as well as other toxic compounds that inhibit cholinesterase activity, in fruits, vegetables, and other agricultural commodities. The kit is based on a cholinesterase inhibition assay [90] and has a detection limit of 0.05 mg/kg, expressed as trichlorfon equivalents. The sensitivity, specificity, and accuracy of the GT Test Kit are 92.3%, 85.1%, and 87.1%, respectively [91].

Scheme 1 presents a schematic illustration of the experimental procedure used to assess pesticide residues using the "GT" Pesticide Test Kit. Briefly, each homogenized mandarin sample (5 g) was extracted with 10 mL of Solvent No. 1 by continuous mixing for 1 min and left undisturbed for another 15 min or until a clear solvent layer was observed. Subsequently, 2 mL of each sample extract was mixed with 1 mL of Solvent No. 2 and evaporated in an evaporation basin until the residual Solvent No. 1 (the bottom layer) had been completely removed. The resulting sample extract was retained in Solvent No. 2. For the cut-point and the control reference solutions, 0.5 mL of Solvent No. 2 was used for each solution.

To detect pesticide residues, the cut-point reference solution, the control reference solution, and the sample extract test tubes were immersed in a water bath at 35 °C. GT-1 reagent (1.00 mL) was then added to each tube, followed by an incubation at room temperature for 10 min. Next, 0.50 mL, 0.50 mL, and 0.75 mL of GT-2 reagent were added to the control reference, the sample extract, and the cut-point reference test tubes, respectively, and all mixtures were incubated at 35 °C for 30 min. After incubation, 2.0 mL of GT-3 reagent was added. Finally, 1.00 mL of GT-4 reagent followed by 1.00 mL of GT-5 reagent was added to the reaction mixture.

The resulting color of each sample solution, ranging from yellow to dark brown, was compared with those of the control and the cut-point reference solutions. The extent of carbamate and organophosphate pesticide residues was classified into three categories based on the degree of cholinesterase inhibition: (1) pesticide residues were considered undetectable when the color of the sample solution was lighter than or comparable to that of the control reference solution; (2) pesticide residues were considered detectable but within the acceptable range for human consumption when the color of the sample

solution was darker than that of the control reference solution but lighter than that of the cut-point reference solution; and (3) pesticide residues were considered detectable at an unsafe level when the color of the sample solution was darker than that of the cut-point reference solution.



Scheme 1. Schematic representation of sample extraction, solvent exchange, cholinesterase-inhibition analysis using the GT Pesticide Test Kit, and qualitative classification of pesticide residues in mandarin samples as not detected, acceptable, or unsafe based on color comparison with the control and cut-point reference solutions.

2.7.9. Quantification of Pesticide Residues

Profenofos and acetamiprid residues in as-purchased mandarin oranges and P-ManOr samples were extracted using the QuEChERS method specified in EN 15662:2018 and quantified by GC–MS/MS and LC–MS/MS analyses, respectively [92]. Chlorothalonil residues were determined using an in-house method based on AOAC Official Method 2007.01 (2023). Each analytical sample comprised approximately 500 g of whole fruit (peel and pulp) after removal of the stems. All analyses were performed by Central Laboratory (Thailand) Co., Ltd. (Bangkok, Thailand). The limits of detection (LODs) for profenofos, acetamiprid, and chlorothalonil were each 0.005 mg/kg. Acetamiprid was detected in the as-purchased mandarins at a concentration below 0.01 mg/kg, whereas profenofos and chlorothalonil were not detected. Following pretreatment with sodium carbonate, none of the three pesticide residues was detected in the P-ManOr samples.

Acetamiprid residues in the Acet_P-ManOr1, Acet_P-ManOr7, Acet_OA-ManOr1, Acet_OA-ManOr7, and Acet_SR_OA-ManOr1 samples were quantified using the in-house method TM-CH-149 (LC–MS/MS), which is based on AOAC Official Method 2007.01

(2023). Chlorothalonil residues in the Ctnl_P-ManOr1, Ctnl_P-ManOr7, Ctnl_OA-ManOr1, Ctnl_OA-ManOr7, and Ctnl_SR_OA-ManOr1 samples were quantified using the in-house method TM-CH-237 (GC–MS/MS), which is based on the EURL-SRM method SRM-10. Each analytical sample comprised approximately 500 g of whole fruit (peel and pulp) after removal of the stems. Prior to residue analysis, the composite coating was manually removed from the OA-ManOr samples exposed to acetamiprid or chlorothalonil, without further washing with water. All analyses were performed by the Asia Medical and Agricultural Laboratory and Research Center (AMARC; Bangkok, Thailand). The limits of detection (LODs) for acetamiprid and chlorothalonil were each 0.005 mg/kg. Pesticide residue analyses were performed in triplicate for each treatment, and reductions in pesticide deposition are reported as the mean ± standard deviation of three independent replicates (n = 3).

2.7.10. Statistical Analysis

Apparent water contact angles are reported as the mean ± standard deviation of three independent replicates (n = 3). The effects of OA concentration on the wettability of OA-Bio-$CaCO_3$ powder beds and of OA-Bio-$CaCO_3$ concentration on the wettability of the composite films were evaluated separately using one-way analysis of variance (ANOVA), followed by Tukey's honestly significant difference (HSD) post hoc test [93,94].

Reductions in pesticide deposition are also reported as the mean ± standard deviation of three independent replicates (n = 3). Statistical differences between groups were assessed using a two-sided independent-samples t-test. When the residual pesticide concentration was below the analytical limit of detection of 0.005 mg/kg, the corresponding pesticide reduction was reported as a minimum estimate rather than an exact value. Therefore, inferential statistical comparisons involving these estimated values were not performed.

All statistical analyses were conducted using IBM SPSS Statistics, version 28.0, at a 95% confidence level, with statistical significance established at $p < 0.05$.

3. Results and Discussion

3.1. Morphological Characterization of C-GMS (RM) and Bio-$CaCO_3$ Particles

Waste green mussel (*Perna viridis*) shells were sequentially subjected to alkaline treatment with KOH, thermal treatment, mechanical pulverization using an electric grinder, bleaching with H_2O_2, and high-speed grinding to produce a fine, unsieved Bio-$CaCO_3$ (NSif) powder. The particle morphology of Bio-$CaCO_3$ (NSif) was examined and compared with that of the initial C-GMS (RM) powder. Figure 1 presents field-emission scanning electron microscopy (FE-SEM) micrographs of the C-GMS (RM) and Bio-$CaCO_3$ particles. The C-GMS (RM) powder exhibited stratified particles (Figure 1A), indicating that mechanical pulverization alone fragmented the nacreous shell structure without disintegrating it into individual pseudo-hexagonal aragonite tablets [76]. A similar morphology has previously been reported for ground green mussel shells by Lertwattanaruk et al. [95]. In contrast, Bio-$CaCO_3$ (NSif) consisted predominantly of discrete, pseudo-hexagonal aragonite tablets (Figure 1C). The removal of the organic matrix through sequential KOH treatment, thermal treatment at 200 °C, and H_2O_2 bleaching likely weakened the shell structure, thereby facilitating its disintegration into individual aragonite tablets during mechanical grinding [96]. As shown in Figure 1D, the characteristic particle morphology of Bio-$CaCO_3$ was retained after sieving to obtain Bio-$CaCO_3$ (Sif). Similarly, sieving did not substantially alter the characteristic morphology of the C-GMS (RM) particles (Figure 1B).

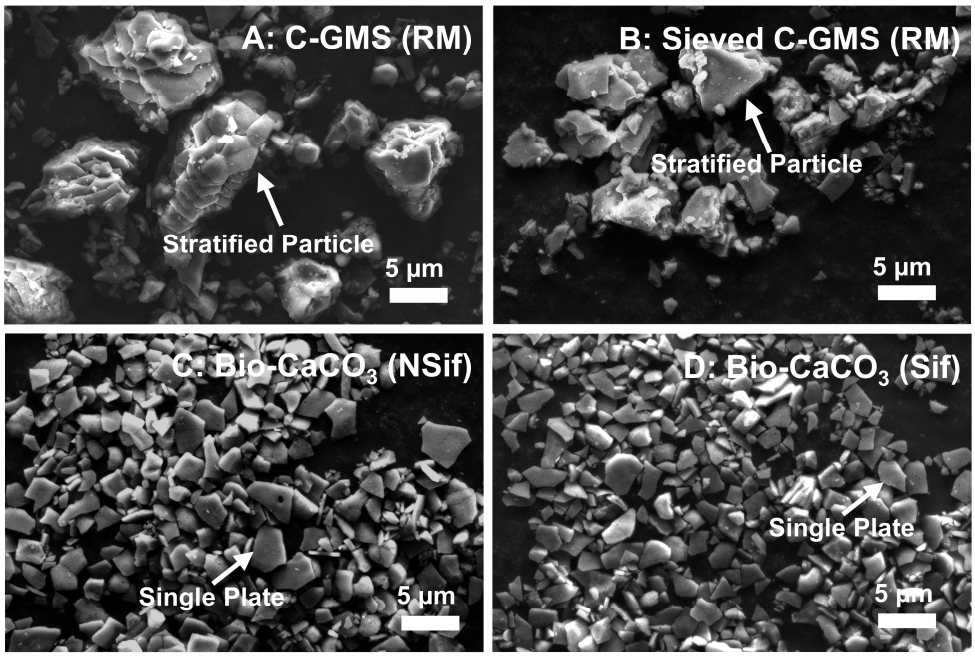


Figure 1. FE-SEM micrographs of pulverized green mussel shell powders [C-GMS (RM)] before (**A**) and after (**B**) sieving through a 200-mesh sieve, and extracted Bio-$CaCO_3$ powders before [Bio-$CaCO_3$ (NSif); (**C**)] and after [Bio-$CaCO_3$ (Sif); (**D**)] sieving. Scale bars represent 5 μm.

3.2. Crystal Structures of C-GMS (RM) and Bio-$CaCO_3$ (Sif) Particles

Figure 2 presents the X-ray diffractograms of the extracted Bio-$CaCO_3$ (Sif) particles in comparison with the starting C-GMS (RM) powders. Table 7 summarizes the diffraction plane assignments for C-GMS (RM) and Bio-$CaCO_3$ (Sif) powders, which were determined by comparing the experimental *d*-spacing values with the theoretical values calculated for orthorhombic aragonite $CaCO_3$ crystals.

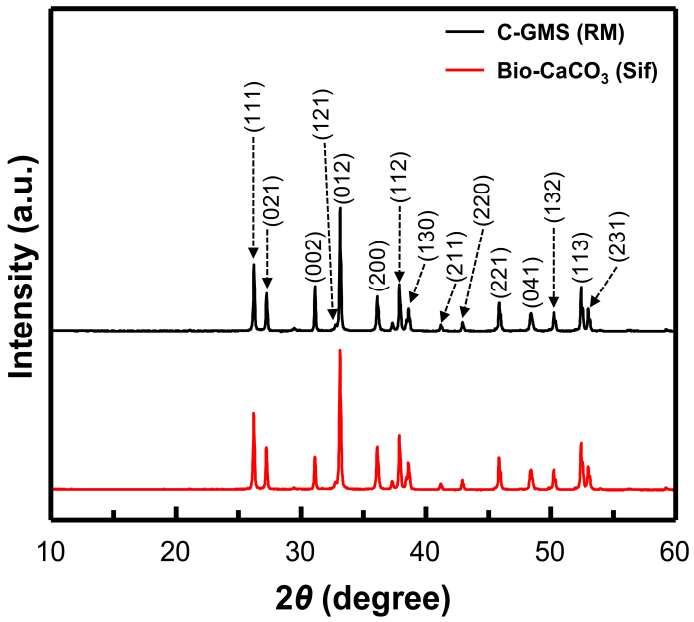


Figure 2. X-ray diffraction patterns of the starting C-GMS (RM) powder (black line) and the extracted Bio-$CaCO_3$ (Sif) powder (red line).

Table 7. X-ray diffraction peak assignments for C-GMS (RM) and extracted Bio-$CaCO_3$ (Sif) powders.

Diffraction Planes	Calculated *d*-Spacing		
	Theoretical *d*-Spacing Calculation Based on Orthorhombic System (Å)	Bragg's Law	
		C-GMS (RM) Powder (2θ/°, *d*-Spacing/Å)	Extracted Bio-$CaCO_3$ (Sif) Powder (2θ/°, *d*-Spacing/Å)
(111)	3.40	26.24°, 3.39	26.22°, 3.40
(021)	3.27	27.26°, 3.27	27.24°, 3.27
(002)	2.87	31.12°, 2.87	31.11°, 2.87
(121)	2.73	32.78°, 2.73	32.76°, 2.73
(012)	2.70	33.13°, 2.70	33.12°, 2.70
(200)	2.48	36.11°, 2.49	36.09°, 2.49
(112)	2.37	37.89°, 2.37	37.88°, 2.37
(130)	2.34	38.62°, 2.33	38.61°, 2.33
(211)	2.19	41.20°, 2.19	41.18°, 2.19
(220)	2.11	42.93°, 2.11	42.91°, 2.11
(221)	1.98	45.87°, 1.98	45.85°, 1.98
(041)	1.88	48.41°, 1.88	48.42°, 1.88
(132)	1.81	50.24°, 1.81	50.22°, 1.82
(113)	1.74	52.42°, 1.74	52.42°, 1.74
(231)	1.73	52.99°, 1.73	52.99°, 1.73

The C-GMS (RM) and the extracted Bio-$CaCO_3$ (Sif) powders exhibited closely matching diffraction-peak positions and *d*-spacing values that agreed well with those theoretically calculated for orthorhombic aragonite (Table 7). The X-ray diffraction pattern of the extracted Bio-$CaCO_3$ (Sif) particles closely resembled that of the initial green mussel shell powders. The negligible shifts in the diffraction peak positions following extraction indicated that the process did not alter the original crystal structure of the C-GMS (RM) particles and that the orthorhombic aragonite crystal polymorph was preserved in the extracted Bio-$CaCO_3$ (Sif) particles.

Furthermore, the extracted Bio-$CaCO_3$ (Sif) particles primarily exhibited the aragonite crystal polymorph because the characteristic diffraction peak corresponding to the (104) diffraction plane of the calcite polymorph at 2θ of 29.4132° was not observed in their X-ray diffraction pattern. The molar fraction of aragonite polymorph in the extracted Bio-$CaCO_3$ (Sif) particles was estimated to be 97.2 mol%, whereas that of the C-GMS (RM) particles was approximately 95.7 mol% [97]. These values are consistent with the previously reported weight percentage of the aragonite phase in green mussel shells [98].

3.3. Particle Size Distributions of C-GMS (RM) and Bio-$CaCO_3$ (Sif) Particles

Volume-based size distributions of the C-GMS (RM) and extracted Bio-$CaCO_3$ (Sif) powders were characterized using laser diffraction. The results are shown in Figure 3.

Particle size distribution analysis revealed clear differences between the C-GMS (RM) powder and the extracted Bio-$CaCO_3$ (Sif). The C-GMS (RM) powder exhibited a broad and multimodal distribution, with particle populations extending from the low micrometer range to above 1000 µm. This broad profile indicates substantial particle heterogeneity, which is expected for mechanically ground shell materials [99]. In contrast, the extracted Bio-$CaCO_3$ (Sif) showed a narrower particle size distribution, with the main population concentrated at smaller size classes and a marked reduction in coarse particles. The large-particle fraction was effectively removed after sieving through a 200-mesh sieve, yielding finer Bio-$CaCO_3$ (Sif) particles. The D[4,3] values of the C-GMS (RM) powders and the refined extracted Bio-$CaCO_3$ (Sif) powders were determined to be 123.67 ± 8.08 and

34.47 ± 2.29 µm, respectively. This represents an approximately 72% reduction in *D*[4,3] values after the extraction and refining process. The *D*[3,2] values of the C-GMS (RM) and the Bio-$CaCO_3$ (Sif) particles were 5.62 ± 0.03 and 6.50 ± 0.04 µm, respectively. Additionally, the average length-based diameter of the Bio-$CaCO_3$ (Sif) particles was determined directly from the SEM micrographs to be 2.55 ± 0.72 µm. Although C-GMS (RM) exhibited a slightly lower *D*[3,2], its substantially higher *D*[4,3] indicates a heterogeneous particle size distribution containing both fine fragments and coarse, incompletely pulverized particles. Processing and sieving preferentially removed the coarse-particle tail of Bio-$CaCO_3$ (Sif), markedly decreasing *D*[4,3] while slightly increasing *D*[3,2], rather than uniformly reducing all particle size parameters [100].

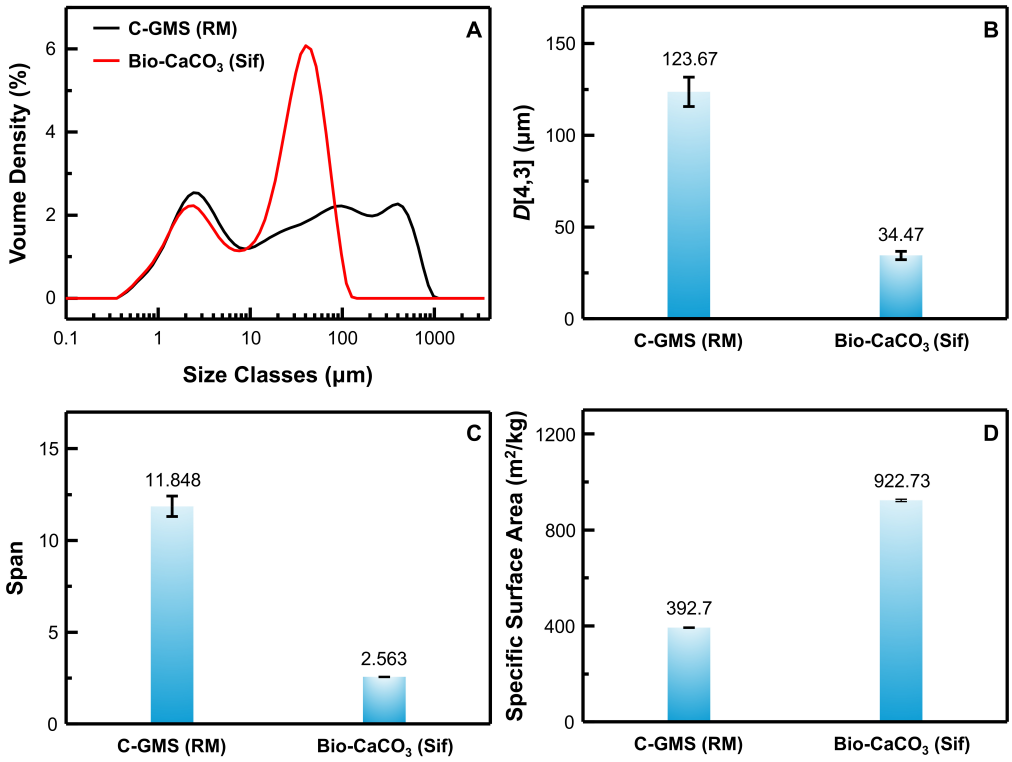


Figure 3. Volume-based particle size characteristics of the C-GMS (RM) powder and the extracted Bio-$CaCO_3$ (Sif): particle size distributions expressed as volume density as a function of particle size (**A**); volume-weighted mean particle diameter, *D*[4,3] (**B**); distribution span (**C**); and specific surface area (**D**). Data in (**B**–**D**) are presented as the mean ± standard deviation of three independent experiments (n = 3).

The span value reflecting the width of the particle size distribution [101] decreased markedly from 11.848 ± 0.557 for the C-GMS (RM) powder to 2.563 ± 0.028 for the Bio-$CaCO_3$ (Sif) powder (Figure 3C). The high span value of the C-GMS (RM) powder indicates a highly polydisperse system, consistent with the broad distribution observed in the particle size curve. In contrast, the considerably lower span value of the Bio-$CaCO_3$ (Sif) powder demonstrates a much narrower and more homogeneous particle size distribution. In addition to size reduction and improved uniformity, the extraction and refining process substantially increased the specific surface area (Figure 3D). The specific surface area increased from 392.70 ± 2.34 m^2/kg for the C-GMS (RM) powder to 922.73 ± 4.88 m^2/kg for the refined Bio-$CaCO_3$ (Sif) powder, corresponding to an approximately 2.35-fold enhancement. This increase in surface area is consistent with the observed reduction in particle size [102]. The increased specific surface area of the Bio-$CaCO_3$ (Sif) particles is particularly beneficial for subsequent functionalization with OA [103].

3.4. Molecular Characterization

The successful immobilization of OA on the OA-Bio-$CaCO_3$ surface was evaluated using ATR FT-IR spectroscopy and X-ray photoelectron spectroscopy (XPS). The ATR FT-IR spectra of Bio-$CaCO_3$ (Sif) and OA-Bio-$CaCO_3$ are presented in Figure 4. The IR absorption bands of Bio-$CaCO_3$ (Sif) at 1787, 1456, and 864 cm^{-1}, together with the doublet 711/701 cm^{-1}, were assigned to the combination of symmetric stretching and C–O in-plane bending, antisymmetric stretching, out-of-plane bending, and characteristic C–O in-plane bending vibrations of aragonite $CaCO_3$, respectively [104]. Following OA functionalization, these characteristic aragonite bands remained detectable in the OA-Bio-$CaCO_3$ spectrum at 1787, 1469, 865, and 707/701 cm^{-1}, respectively. Neat OA exhibited IR absorption bands at 2922, 2856, and 1714 cm^{-1}, corresponding to asymmetric CH_2 stretching, symmetric CH_2 stretching, and C=O stretching vibrations, respectively [105]. OA-Bio-$CaCO_3$ also exhibited IR absorption peaks at 2926 and 2853 cm^{-1}, supporting the presence of oleic acid-derived hydrocarbon chains on the particle surfaces. Oleate anions can form hydrophobic, chemisorbed layers on aragonite $CaCO_3$ through interactions between carboxylate groups and surface-exposed Ca^{2+} sites [106]. However, earlier studies of fatty-acid-coated $CaCO_3$ also indicate that chemically bound and physically adsorbed surface species can coexist, particularly when modification occurs in an aqueous medium [107].

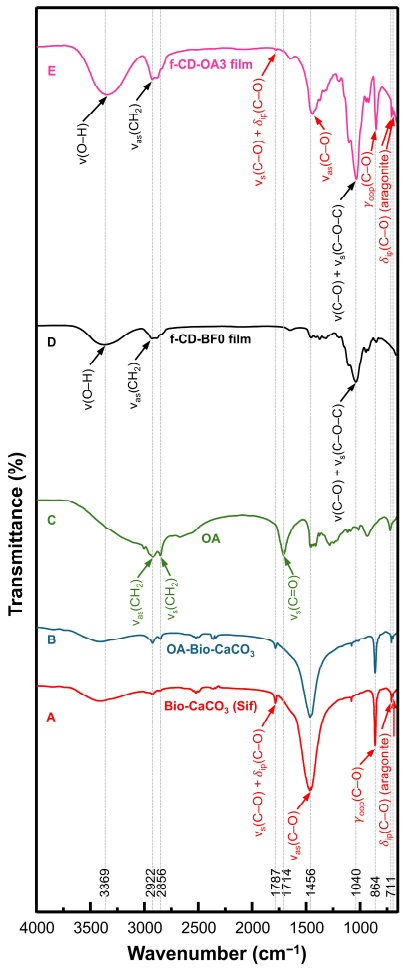


Figure 4. ATR FT-IR spectra of Bio-$CaCO_3$ (Sif) (**A**), OA-Bio-$CaCO_3$ (**B**), oleic acid (OA) (**C**), an unfilled HPMC-glycerol (Gro) film (f-CD-BF0) (**D**), and an HPMC-glycerol (Gro) film cast from a coating dispersion containing 20% (*w*/*v*) OA-Bio-$CaCO_3$ (f-CD-OA3) (**E**). Vibrational-mode notation: ν, stretching; ν_s, symmetric stretching; ν_{as}, antisymmetric stretching; δ_{ip}, in-plane bending; γ_{oop}, out-of-plane bending.

Fine OA-Bio-$CaCO_3$ powders were incorporated into an HPMC solution to prepare a composite coating dispersion. The ATR FT-IR spectrum of the f-CD-BF0 film displayed absorption bands at 3369, 2931, and 1040 cm^{-1}, assigned to O–H stretching, predominantly antisymmetric CH_2 stretching, and overlapping C–O and symmetric C–O–C stretching vibrations of the polysaccharide framework, respectively [108,109]. The ATR FT-IR spectrum of the f-CD-OA3 film exhibited characteristic aragonite $CaCO_3$ bands at 1786 cm^{-1} and a doublet at 710/699 cm^{-1}, supporting the successful incorporation of OA-Bio-$CaCO_3$ into the polymer matrix. Additionally, the IR absorption bands of OA-Bio-$CaCO_3$ at 1469 and 865 cm^{-1} shifted to lower wavenumbers, appearing at 1444 and 855 cm^{-1}, respectively, after incorporation into the HPMC film. These red shifts suggest interfacial interactions between the organic polymer matrix and the mineral surface [110]. The base HPMC-Gro polymer matrix of the f-CD-OA3 film exhibited characteristic O–H stretching vibrations, antisymmetric CH_2 stretching, and overlapping C–O and C–O–C vibrations at 3352, 2931, and 1039 cm^{-1}, respectively.

3.5. XPS Characterization of Bio-$CaCO_3$ (Sif) and OA-Bio-$CaCO_3$ Particles

To further confirm the presence of oleate molecules on OA-Bio-$CaCO_3$ surfaces, X-ray photoelectron spectroscopy was utilized for probing the surface composition of OA-Bio-$CaCO_3$ in comparison to Bio-$CaCO_3$ (Sif) [111]. The survey-scan XPS spectrum of Bio-$CaCO_3$ (Sif) revealed C, O, and Ca as the predominant surface elements, with atomic concentrations of 49.09, 40.74, and 9.83% (atom), respectively (Figure 5). In comparison, the OA-Bio-$CaCO_3$ contained 53.62, 35.04, and 8.95% (atom) of C, O, and Ca, respectively. Following OA functionalization, the surface carbon concentration increased by 4.53 percentage points, whereas the oxygen and calcium concentrations decreased by 5.70 and 0.88 percentage points, respectively. Accordingly, the C/Ca atomic ratio increased from approximately 4.99 for Bio-$CaCO_3$ (Sif) to 5.99 for OA-Bio-$CaCO_3$, while the C/O ratio increased from approximately 1.20 to 1.53. These changes support the immobilization of a carbon-rich organic layer from OA onto Bio-$CaCO_3$ (Sif) surfaces. However, some trace elements in negligible amounts, including 0.33% (atom) Na in Bio-$CaCO_3$ (Sif) and 1.82% (atom) N and 0.57% (atom) Si in OA-Bio-$CaCO_3$, were detected. Because these elements are not constituents of OA, they were considered trace surface-associated species rather than evidence of the functionalization mechanism.

Interfacial bonding characteristics were further evaluated using the corresponding high-resolution C 1s, O 1s, and Ca 2p core-level spectra. Clear changes in the relative intensities and fitted components of the high-resolution spectra of C 1s, O 1s, and Ca 2p were observed, demonstrating an alteration of the Bio-$CaCO_3$ surface chemistry after surface functionalization with OA [112] (Figures 6–8). The high-resolution Ca 2p spectra of Bio-$CaCO_3$ (Sif) and OA-Bio-$CaCO_3$ displayed the characteristic Ca $2p_{1/2}$ and Ca $2p_{3/2}$ doublet (Figure 6A), attributed to Ca^{2+} [113]. For Bio-$CaCO_3$ (Sif), the principal peaks were located at binding energies of 350.87 and 347.32 eV, respectively, with a spin–orbit separation of 3.55 eV. The observed binding energies and Ca 2p spin–orbit splitting were consistent with previously reported values [114]. Following OA modification, these peaks shifted slightly to 351.10 and 347.56 eV, corresponding to a positive shift of approximately 0.23–0.24 eV. The relative peak areas remained comparable following OA functionalization. The Ca $2p_{1/2}$ component contributed 29.23% and 29.83% of the fitted Ca 2p envelopes of Bio-$CaCO_3$ (Sif) and OA-Bio-$CaCO_3$, respectively, whereas the corresponding Ca $2p_{3/2}$ contributions were 67.08% and 65.99% (Figure 6B–D). The minor peaks detected at higher binding energies were assigned to weak satellite or energy-loss features and were not considered primary calcium chemical states [115]. The small positive shift in the principal Ca 2p doublet suggests a change in the electronic environment of surface calcium ions [116].

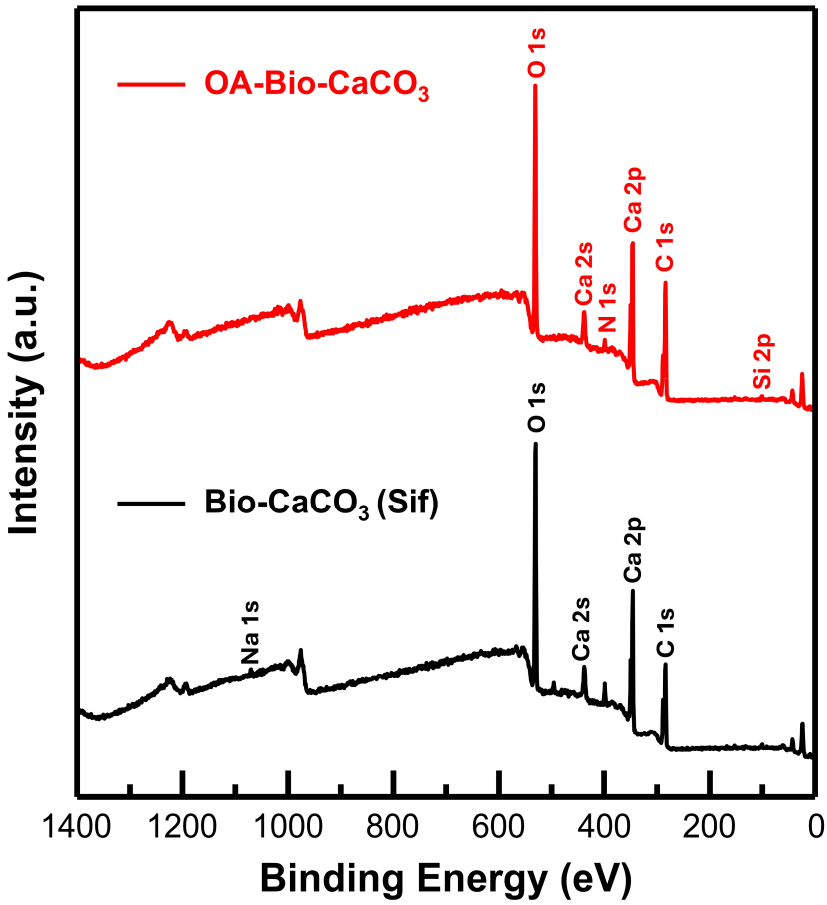


Figure 5. Wide-scan XPS spectra of Bio-$CaCO_3$ (Sif) and oleic acid-functionalized Bio-$CaCO_3$ (OA-Bio-$CaCO_3$).

Further evidence of surface modification was obtained from the C 1s (Figure 7) and O 1s core-level spectra (Figure 8). The C 1s spectrum of Bio-$CaCO_3$ (Sif) was deconvoluted into components centered at 285.00, 286.20, 287.23, 288.30, and 289.59 eV, which were assigned to C–C/C–H, C–O/C–O–C, C=O/O–C–O, O–C=O/C(=O)OH, and carbonate functional groups, respectively (Figure 7B) [112]. Following OA functionalization, the relative contribution of the aliphatic C–C/C–H component increased from 48.95% for Bio-$CaCO_3$ (Sif) to 57.50% for OA-Bio-$CaCO_3$, with the corresponding peak centered at 284.91 eV (Figure 7C,D). This increase is consistent with the introduction of the long hydrocarbon chain of OA. The components assigned to carbonyl- or carboxyl-containing species, centered at 288.30 eV for Bio-$CaCO_3$ (Sif) and 288.25 eV for OA-Bio-$CaCO_3$, accounted for 5.41% and 6.72% of the total C 1s peak area, respectively (Figure 7D). In parallel, the relative contribution of carbonate carbon decreased from 27.87% at 289.59 eV for Bio-$CaCO_3$ (Sif) to 21.25% at 289.88 eV for OA-Bio-$CaCO_3$. The increased relative contribution of carbonyl- and carboxyl-containing species, together with the concomitant decrease in the carbonate contribution, is consistent with partial coverage of the mineral surface by an organic layer.

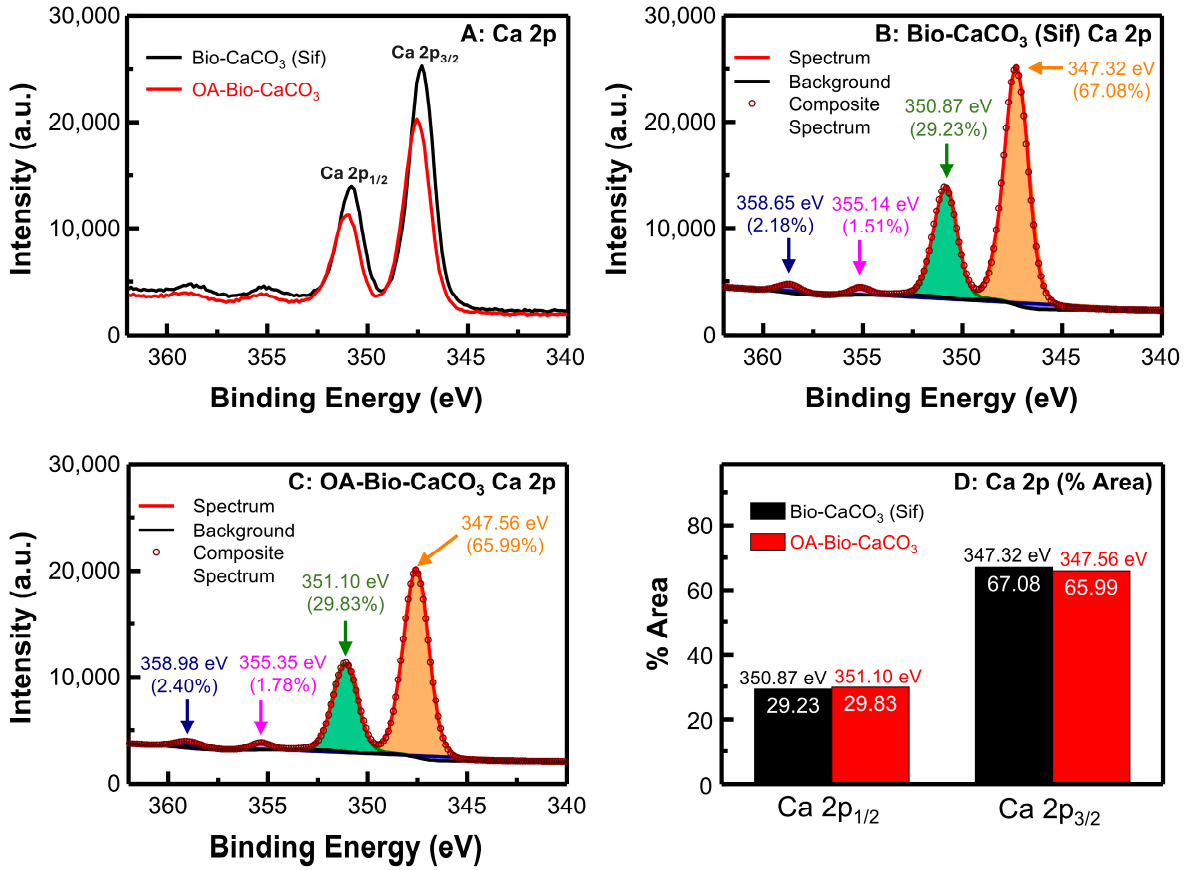


Figure 6. High-resolution Ca 2p XPS spectra of Bio-$CaCO_3$ (Sif) and oleic acid-functionalized Bio-$CaCO_3$ (OA-Bio-$CaCO_3$): Comparative Ca 2p core-level spectra (**A**); peak-deconvoluted Ca 2p spectra of Bio-$CaCO_3$ (Sif) (**B**) and OA-Bio-$CaCO_3$ (**C**); and relative areas of selected fitted components at their corresponding binding energies (**D**). In (**A**), black and red solid lines represent Bio-$CaCO_3$ (Sif) and OA-Bio-$CaCO_3$, respectively. In (**B**,**C**), red solid lines represent the experimental spectra, black solid lines indicate the background signals, and open dark-red circles represent the composite fitting envelopes (composite spectra). Orange and green shaded peaks correspond to the principal Ca $2p_{3/2}$ and Ca $2p_{1/2}$ components, respectively, whereas magenta and dark blue shading identifies additional fitted components at approximately 355 and 359 eV, respectively. Corresponding colored arrows and annotations indicate the binding energies and relative peak areas of these components. In (**D**), black and red bars represent Bio-$CaCO_3$ (Sif) and OA-Bio-$CaCO_3$, respectively; values within the bars indicate relative peak areas (%), and labels above the bars indicate the corresponding binding energies.

The high-resolution O 1s spectra of Bio-$CaCO_3$ (Sif) and OA-Bio-$CaCO_3$ are presented in Figure 8.

For Bio-$CaCO_3$ (Sif), the O 1s spectrum was deconvoluted into three components centered at 531.36 eV (51.45%), 531.91 eV (38.48%), and 533.21 eV (10.07%) (Figure 8B). By contrast, the O 1s spectrum of OA-Bio-$CaCO_3$ required four fitted components at 530.85 (6.56%), 531.53 (41.44%), 532.17 (42.77%), and 533.16 eV (9.23%) (Figure 8C). The binding energies of 531.36 eV for Bio-$CaCO_3$ (Sif) and 530.85 and 531.53 eV for OA-Bio-$CaCO_3$ could correspond to the lattice oxygen in $CaCO_3$ (Figure 8D) [115]. The additional low-binding-energy component at 530.85 eV of OA-Bio-$CaCO_3$ may indicate a modified local environment of oxygen species coordinated with calcium at the mineral–organic interface. The components centered at a binding energy of 531.91 eV for Bio-$CaCO_3$ (Sif) may be associated with the physisorbed/chemisorbed oxygen species [115]. The components centered at a binding energy of 531.53 eV for OA-Bio-$CaCO_3$ may also be assigned to C=O and O–C=O groups originating from carboxylic acids, carboxylates, or carbonyl-

containing species [117]. The redistribution of the O 1s envelope, particularly the increased contribution of the component at 532.17 eV, is consistent with the formation of additional oxygen-containing surface species following OA functionalization [118]. When considered together with the corresponding C 1s and ATR FT-IR results, this change supports the presence of oleate-derived carboxyl/carboxylate species on the OA-Bio-$CaCO_3$ surface. The components centered at 533.21 and 533.16 eV for Bio-$CaCO_3$ (Sif) and OA-Bio-$CaCO_3$, respectively, exhibited comparable relative areas and may be attributed to organic matter inherently associated with the Bio-$CaCO_3$ matrix [117].

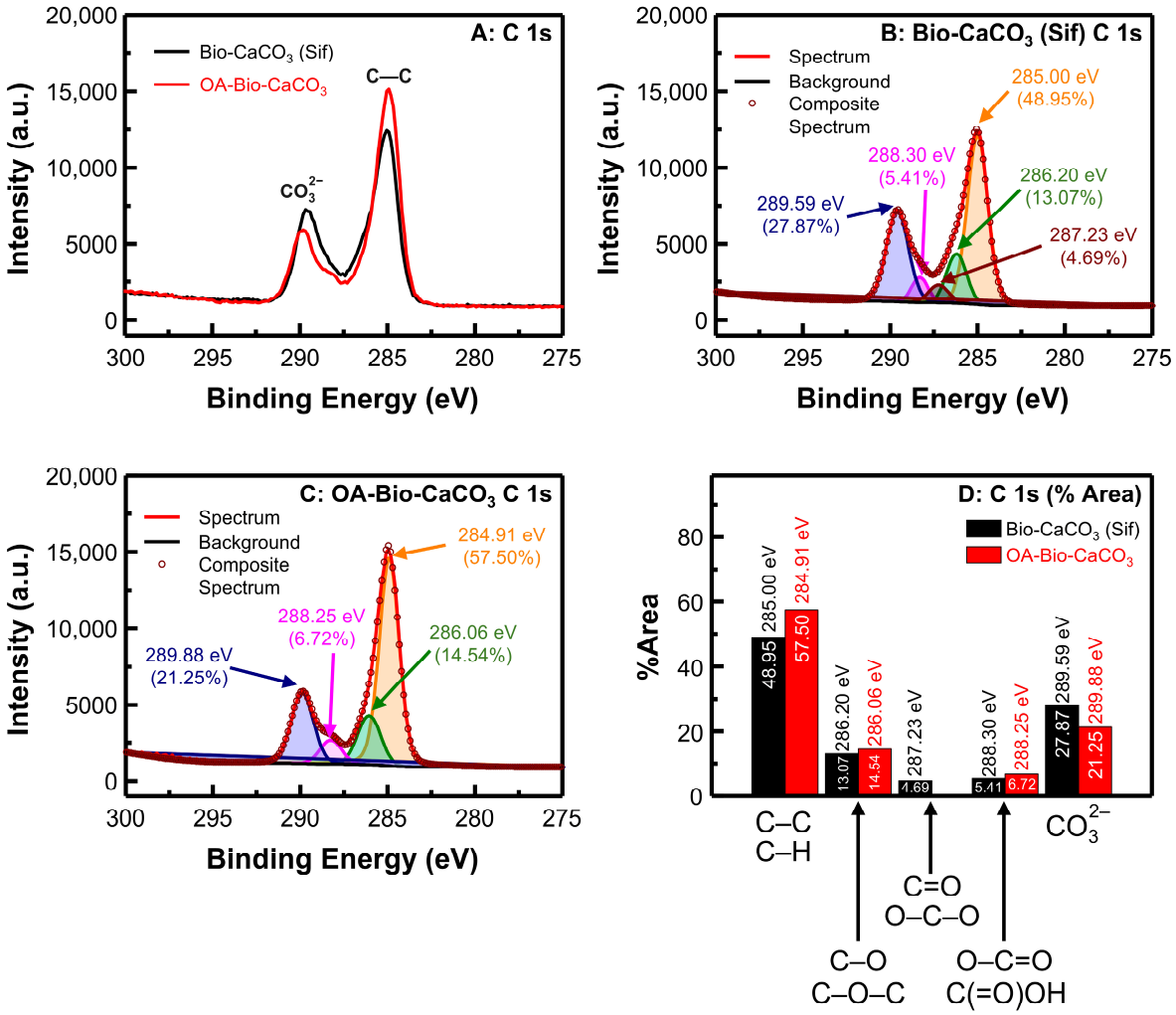


Figure 7. High-resolution C 1s XPS spectra of Bio-$CaCO_3$ (Sif) and oleic acid-functionalized Bio-$CaCO_3$ (OA-Bio-$CaCO_3$): Comparative C 1s core-level spectra (**A**); peak-deconvoluted C 1s spectra of Bio-$CaCO_3$ (Sif) (**B**) and OA-Bio-$CaCO_3$ (**C**); and relative areas of selected fitted components at their corresponding binding energies (**D**). In (**A**), black and red solid lines represent Bio-$CaCO_3$ (Sif) and OA-Bio-$CaCO_3$, respectively. In (**B**,**C**), red solid lines represent the experimental spectra, black solid lines indicate the background signals, and open dark-red circles represent the composite fitting envelopes (composite spectra). Orange, green, magenta, and blue shaded components are assigned to C–C/C–H, C–O/C–O–C, O–C=O/C(=O)OH, and carbonate (CO_3^{2-}), respectively. The additional dark-red component in (B) is assigned to C=O/O–C–O. Corresponding colored arrows and annotations indicate the binding energies and relative peak areas of the fitted components. In (**D**), black and red bars represent Bio-$CaCO_3$ (Sif) and OA-Bio-$CaCO_3$, respectively; labels above and within the bars indicate binding energies and relative peak areas (%), respectively; the labels and black arrows below the bars identify the corresponding chemical assignments.

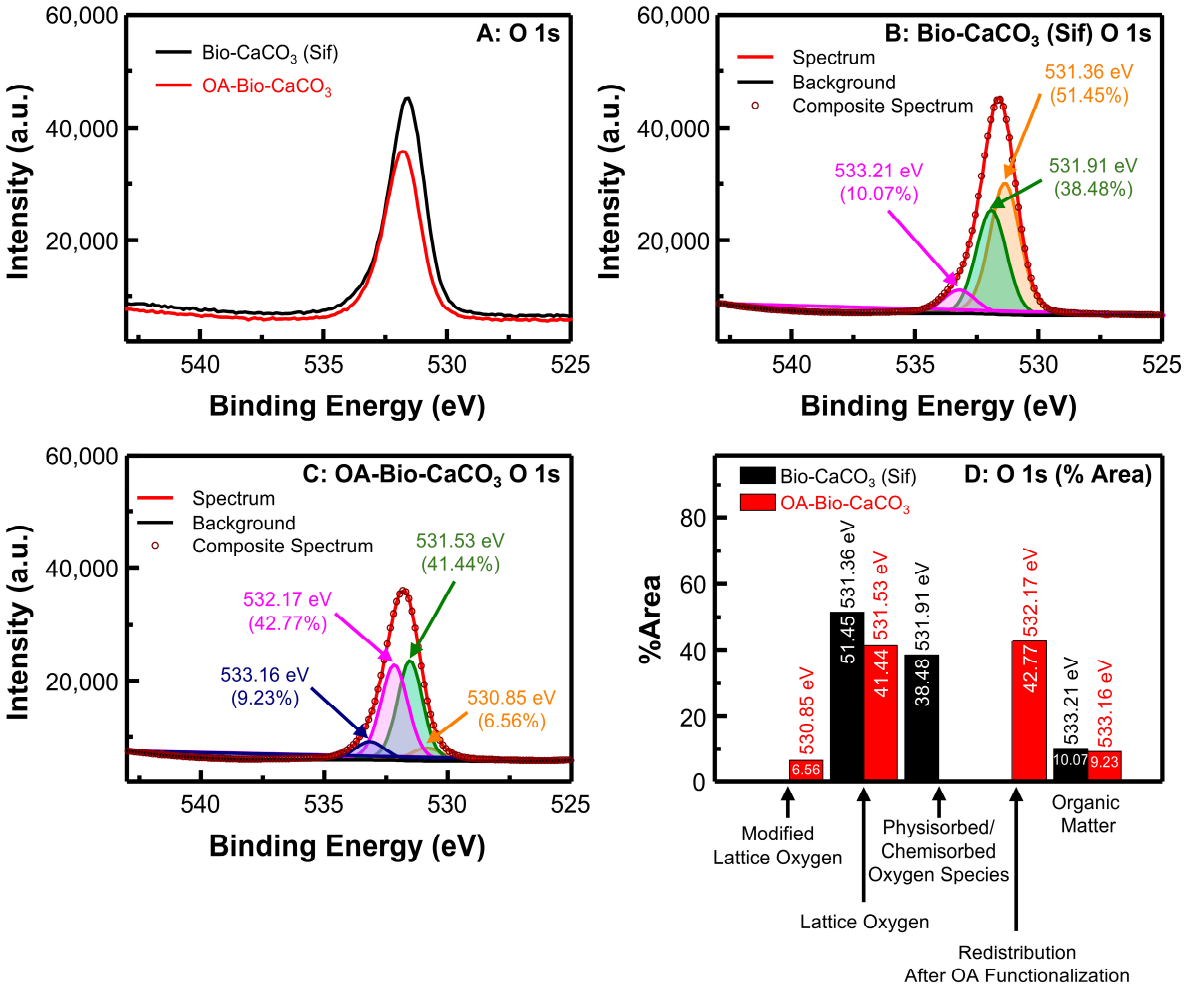


Figure 8. High-resolution O 1s XPS spectra of Bio-$CaCO_3$ (Sif) and oleic acid-functionalized Bio-$CaCO_3$ (OA-Bio-$CaCO_3$): Comparative O 1s core-level spectra (**A**); peak-deconvoluted O 1s spectra of Bio-$CaCO_3$ (Sif) (**B**) and OA-Bio-$CaCO_3$ (**C**); and relative areas of selected fitted components at their corresponding binding energies (**D**). In (**A**), black and red solid lines represent Bio-$CaCO_3$ (Sif) and OA-Bio-$CaCO_3$, respectively. In (**B**,**C**), red solid lines represent the experimental spectra, black solid lines indicate the background signals, and open dark-red circles represent the composite fitting envelopes (composite spectra). In (**B**), orange, green, and magenta curves and shaded areas represent fitted components centered at 531.36, 531.91, and 533.21 eV, respectively. In (**C**), orange, green, magenta, and blue curves and shaded areas represent fitted components centered at 530.85, 531.53, 532.17, and 533.16 eV, respectively. In (**D**), black and red bars represent Bio-$CaCO_3$ (Sif) and OA-Bio-$CaCO_3$, respectively; labels above and within the bars indicate binding energies and relative peak areas (%), respectively; the labels and black arrows below the bars identify the corresponding chemical assignments.

3.6. Surface Wetting Properties

The surface wettability of Bio-$CaCO_3$ (Sif) functionalized with 1.0–6.0% (w/v) OA was evaluated and compared with unmodified Bio-$CaCO_3$ (Sif) by measuring the apparent water contact angle. The results are presented in Figure 9. The Bio-$CaCO_3$ (Sif) powder exhibited a low apparent water contact angle of 25.2° ± 12.0°, confirming the intrinsically hydrophilic nature of the aragonite $CaCO_3$ surface [119]. OA functionalization markedly altered the wetting characteristics of the Bio-$CaCO_3$ (Sif) powder. The apparent water contact angle of Bio-$CaCO_3$ (Sif) modified with 1.0% (w/v) OA increased sharply to 134.9° ± 2.7°. Statistical analysis further revealed a significant difference between unmodified Bio-$CaCO_3$ (Sif) and Bio-$CaCO_3$ (Sif) functionalized with 1.0% (w/v) OA ($p < 0.05$). The apparent

water contact angles of OA-Bio-$CaCO_3$ obtained at OA concentrations of 2.0% and 3.0% (w/v) were 146.4° ± 8.4° and 152.7° ± 2.7°, respectively. The value obtained at an OA concentration of 3.0% (w/v) exceeded the commonly accepted threshold of 150° for superhydrophobic surfaces, indicating that relatively low OA concentrations were sufficient to convert the hydrophilic Bio-$CaCO_3$ (Sif) surface into a strongly water-repellent material. The representative droplet image obtained for the Bio-$CaCO_3$ (Sif) powder modified with 3.0% (w/v) OA further illustrates the formation of a nearly spherical water droplet with limited spreading on the powder surface (Figure 9B). The carboxyl group of OA can interact with calcium-containing surface sites, whereas the long nonpolar hydrocarbon chain is oriented away from the mineral surface, thereby increasing surface hydrophobicity [103]. Increasing the OA concentration beyond 3.0% (w/v) did not further improve surface hydrophobicity. Instead, the apparent water contact angles of OA-Bio-$CaCO_3$ decreased to 145.0° ± 6.0° and 136.2° ± 4.5° at OA concentrations of 4.0% (w/v) and 6.0% (w/v), respectively. Additionally, the droplet image recorded for Bio-$CaCO_3$ (Sif) modified with 6.0% (w/v) OA exhibited greater spreading than that observed for Bio-$CaCO_3$ (Sif) modified with 3.0% (w/v) OA (Figure 9C). A reduction in the apparent water contact angle induced by excessive OA concentrations has also been reported for precipitated $CaCO_3$ [79].

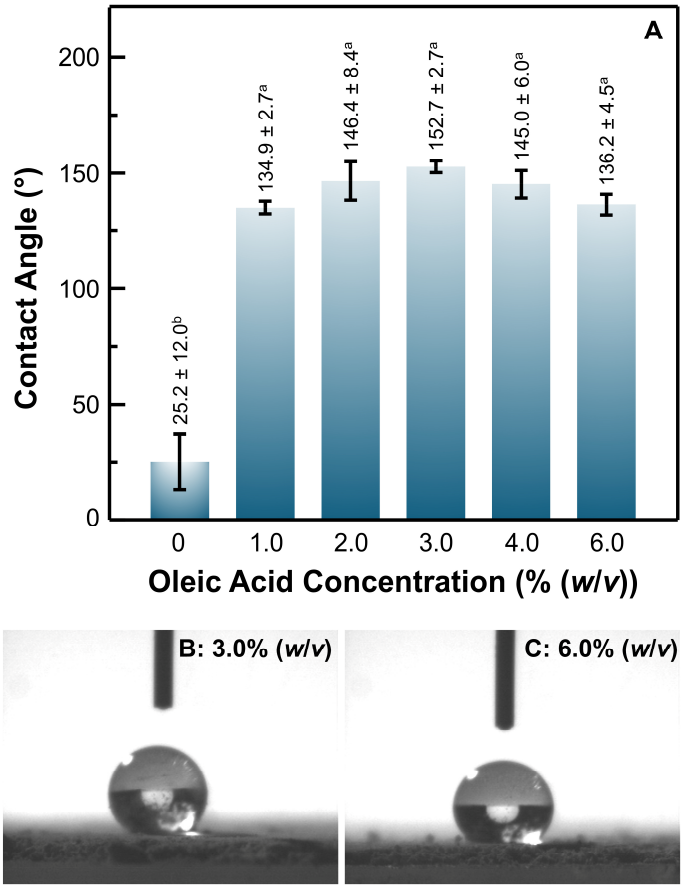


Figure 9. Effect of oleic acid (OA) concentration on the apparent water contact angles of OA-Bio-$CaCO_3$ powder beds. Apparent water contact angles of unmodified Bio-$CaCO_3$ (Sif) and Bio-$CaCO_3$ (Sif) modified with 1.0–6.0% (w/v) OA (**A**). Representative sessile-drop images for Bio-$CaCO_3$ (Sif) powders modified with 3.0% (w/v) OA (**B**) and 6.0% (w/v) OA (**C**). Data are presented as the mean ± standard deviation of three independent experiments (n = 3). Different letters indicate significant differences according to Tukey's HSD test ($p < 0.05$).

Bio-$CaCO_3$ (Sif) functionalized with 3.0% (w/v) OA was selected for subsequent coating experiments because it exhibited the highest mean apparent water contact angle.

However, no statistically significant differences were observed among Bio-$CaCO_3$ (Sif) samples functionalized with 1.0–6.0% (w/v) OA ($p > 0.05$). Hereafter, Bio-$CaCO_3$ (Sif) modified with 3.0% (w/v) OA is designated as OA-Bio-$CaCO_3$ unless otherwise stated. The base coating formulations consisted of HPMC and Gro at a fixed mass ratio of 5:7. Gro was incorporated as a plasticizer to reduce brittleness and enhance the flexibility of the resulting films [120]. OA-Bio-$CaCO_3$ particles were subsequently incorporated into HPMC-Gro matrices to fabricate hydrophobic composite coatings. For comparison, analogous composite films containing unmodified Bio-$CaCO_3$ (Sif), designated f-CD-UM3, were also prepared. The wettability of the resulting films was evaluated by measuring their apparent water contact angles, as presented in Figure 10.

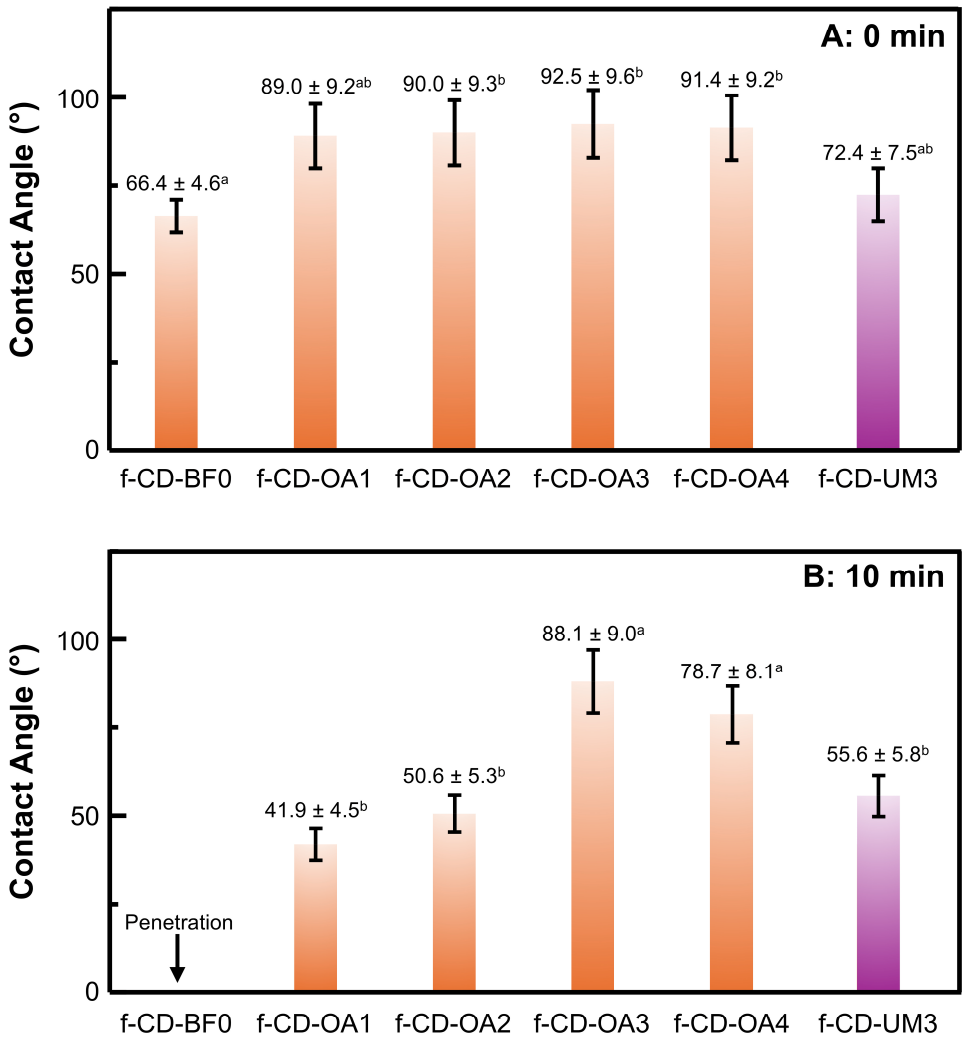


Figure 10. Apparent water contact angles of f-CD-BF0, f-CD-OA1, f-CD-OA2, f-CD-OA3, f-CD-OA4, and f-CD-UM3 films measured 5 s after deposition of the water droplet (0 min) (**A**) and after 10 min (**B**). For f-CD-BF0, "Penetration" indicates that the water droplet had penetrated the film after 10 min. Data are presented as the mean ± standard deviation of three independent experiments ($n = 3$). Different letters indicate significant differences according to Tukey's HSD test ($p < 0.05$).

At 5 s after droplet deposition, the f-CD-BF0 film exhibited an apparent water contact angle of 66.4° ± 4.6°. A pristine HPMC film has been reported to display a water contact angle of 49.3°, indicating its inherent hydrophilicity [121]. Additionally, water contact angles of HPMC in the range of 72–85° have also been reported, depending on the degree of methyl and hydroxypropyl group substitution [122]. Incorporation of Gro into the formulations may increase the hydrophilicity of the film and partially reduce the apparent

water contact angle [123]. The addition of OA-Bio-$CaCO_3$ increased the apparent contact angle to 89.0° ± 9.2°, 90.0° ± 9.3°, 92.5° ± 9.6°, and 91.4° ± 9.2° for f-CD-OA1, f-CD-OA2, f-CD-OA3, and f-CD-OA4 specimens, respectively (Figure 10A). Among the investigated formulations, the f-CD-OA3 sample exhibited the highest initial apparent water contact angle of 92.5° ± 9.6°, indicating a substantially more hydrophobic surface than that of the f-CD-BF0 film. The contact angles of f-CD-OA2, f-CD-OA3, and f-CD-OA4 were significantly higher than that of f-CD-BF0 ($p < 0.05$), whereas f-CD-OA1 and f-CD-UM3 did not differ significantly from either group. The film containing unmodified Bio-$CaCO_3$ (Sif) (f-CD-UM3) exhibited a lower initial contact angle of 72.4° ± 7.5°, demonstrating that OA functionalization was important for improving the surface water repellency of the composite films.

The apparent water contact angles decreased after the water droplets had remained on the film surfaces for 10 min, reflecting time-dependent wetting behavior (Figure 10B). The apparent water contact angle of the f-CD-BF0 film could not be reliably determined after 10 min because the water droplet spread extensively across the film surface, reflecting the inherent hydrophilicity and water susceptibility of the HPMC–Gro matrix. For the f-CD-OA1 and f-CD-OA2 films, the apparent contact angles decreased to 41.9° ± 4.5° and 50.6° ± 5.3°, respectively. By contrast, the f-CD-OA3 and f-CD-OA4 formulations retained relatively high apparent water contact angles of 88.1° ± 9.0° and 78.7° ± 8.1°, respectively, and did not differ significantly from each other ($p > 0.05$). Both values were significantly higher than those obtained for f-CD-OA1, f-CD-OA2, and f-CD-UM3 ($p < 0.05$). The f-CD-UM3 film retained an apparent contact angle of 55.6° ± 5.8°, further confirming that unmodified Bio-$CaCO_3$ (Sif) was less effective than OA-Bio-$CaCO_3$ in maintaining surface water resistance.

The enhanced resistance to wetting exhibited by the f-CD-OA3 and f-CD-OA4 films may be attributed, at least in part, to the lower surface free energy associated with the hydrophobic hydrocarbon chains of OA exposed on the functionalized Bio-$CaCO_3$ surfaces [124]. At lower particle loadings, incomplete surface coverage may have allowed water to interact with and penetrate the hydrophilic HPMC-Gro matrix, accounting for the pronounced time-dependent decreases observed for f-CD-OA1 and f-CD-OA2. These results indicate that the incorporation of an appropriate amount of OA-Bio-$CaCO_3$ not only increased the initial apparent contact angle but also improved the ability of the film surface to maintain water repellency over time. Overall, the f-CD-OA3 film provided the most favorable combination of initial water repellency and resistance to prolonged water contact.

Additionally, representative side-view images of a water droplet deposited on the surface of the f-CD-OA3 film revealed that the water droplet exhibited a well-defined, nearly hemispherical droplet profile 5 s after droplet deposition (Figure 11C). This droplet morphology was largely retained after 10 min of contact with the film surface, indicating limited water spreading and sustained surface water repellency (Figure 11D). These visual observations are consistent with the relatively small decrease in the apparent water contact angle from 92.5° ± 9.6° at 0 min to 88.1° ± 9.0° after 10 min. Although the f-CD-OA1 film also exhibited a rounded droplet profile 5 s after deposition (Figure 11A), the droplet spread substantially after 10 min (Figure 11B). Accordingly, its apparent water contact angle decreased markedly from 89.0° ± 9.2° to 41.9° ± 4.5°. This behavior suggests that a lower OA-Bio-$CaCO_3$ loading was insufficient to maintain a continuous water-repellent surface during prolonged contact with water.

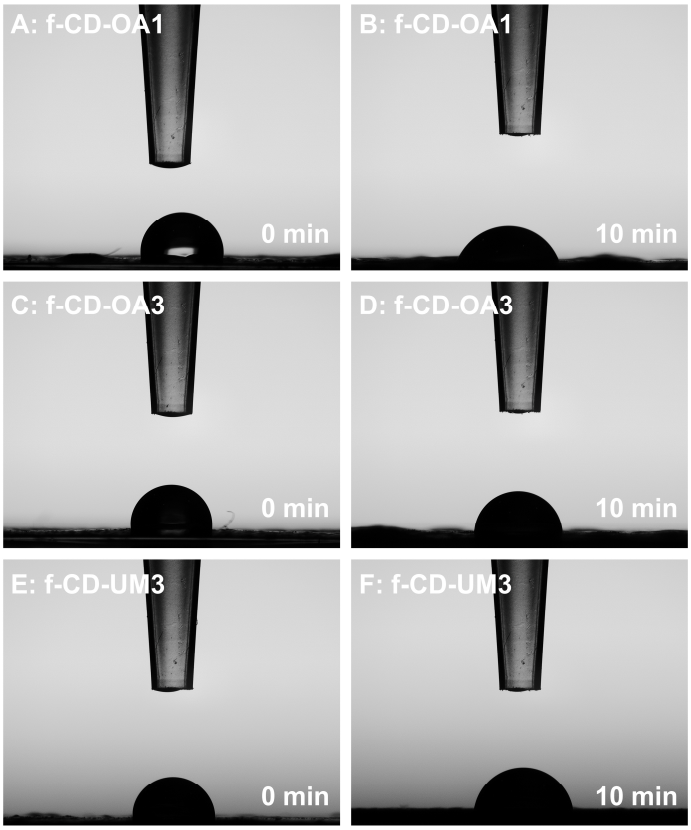


Figure 11. Representative sessile-drop images illustrating the apparent water contact angles of f-CD-OA1 (**A**,**B**), f-CD-OA3 (**C**,**D**), and f-CD-UM3 (**E**,**F**) films 5 s after water-droplet deposition (0 min; (**A**,**C**,**E**)) and after 10 min (**B**,**D**,**F**).

For comparison, the f-CD-UM3 film exhibited apparent water contact angles of 72.4° ± 7.5° at 0 min and 55.6° ± 5.8° after 10 min. These values were lower than those of the f-CD-OA3 film, demonstrating that OA modification played an important role in enhancing the water-repellent properties of the mineral-filled coating. Consistent with these measurements, the water droplet deposited on the film containing unmodified Bio-$CaCO_3$ (Sif) (f-CD-UM3) exhibited flatter profiles than those observed on the OA-Bio-$CaCO_3$-containing film (f-CD-OA3) at the same filler mass concentration at both 0 min (Figure 11E) and 10 min (Figure 11F). These findings confirm that the incorporation of unmodified Bio-$CaCO_3$ (Sif) alone was insufficient to impart sustained water repellency. Accordingly, the CD-OA3 coating formulation was selected for subsequent mandarin-coating applications.

3.7. Morphological Characterization of OA-Bio-$CaCO_3$ Particles and Composite Films

The surface morphology of OA-Bio-$CaCO_3$ particles, the f-CD-OA3 composite film, and the f-CD-UM3 composite film was examined by scanning electron microscopy (SEM) (Figure 12). OA-Bio-$CaCO_3$ retained a polygonal, plate-like morphology (Figure 12A,B) similar to that of unmodified Bio-$CaCO_3$ (Sif) (Figure 1D), indicating that OA modification did not eliminate the intrinsic mineral architecture. Marked differences were observed between the f-CD-OA3 and the f-CD-UM3 composite films. The f-CD-OA3 composite film displayed a heterogeneous and highly porous microstructure, with numerous interconnected voids distributed throughout the polymer matrix (Figure 12C,D). The incorporation of OA-Bio-$CaCO_3$ disrupted the continuity of the HPMC-Gro phase and generated a rougher, more open surface structure. In contrast, the f-CD-UM3 composite film containing Bio-$CaCO_3$ (Sif) at the same mass ratio exhibited a comparatively compact and continuous morphology (Figure 12E,F). Although localized voids remained visible, the surface appeared denser

and less porous than that of the OA-Bio-$CaCO_3$-containing film. This difference may be attributed to the distinct interfacial interactions of the mineral particles with the hydrophilic HPMC-Gro matrix. Bio-$CaCO_3$ (Sif) is hydrophilic and is expected to exhibit a greater affinity for the HPMC-Gro phase, whereas the hydrophobic hydrocarbon chains introduced through OA modification may reduce particle–polymer compatibility and promote the formation of interfacial gaps and pores during film drying [125]. The morphological differences observed by SEM are consistent with the wettability results. The porous and heterogeneous surface of the OA-Bio-$CaCO_3$-containing film may contribute to its enhanced apparent water contact angle by increasing surface roughness and limiting the effective contact area between the water droplet and the solid surface [126,127]. This combined chemical and morphological effect could account for the sustained water repellency of the f-CD-OA3 composite film.

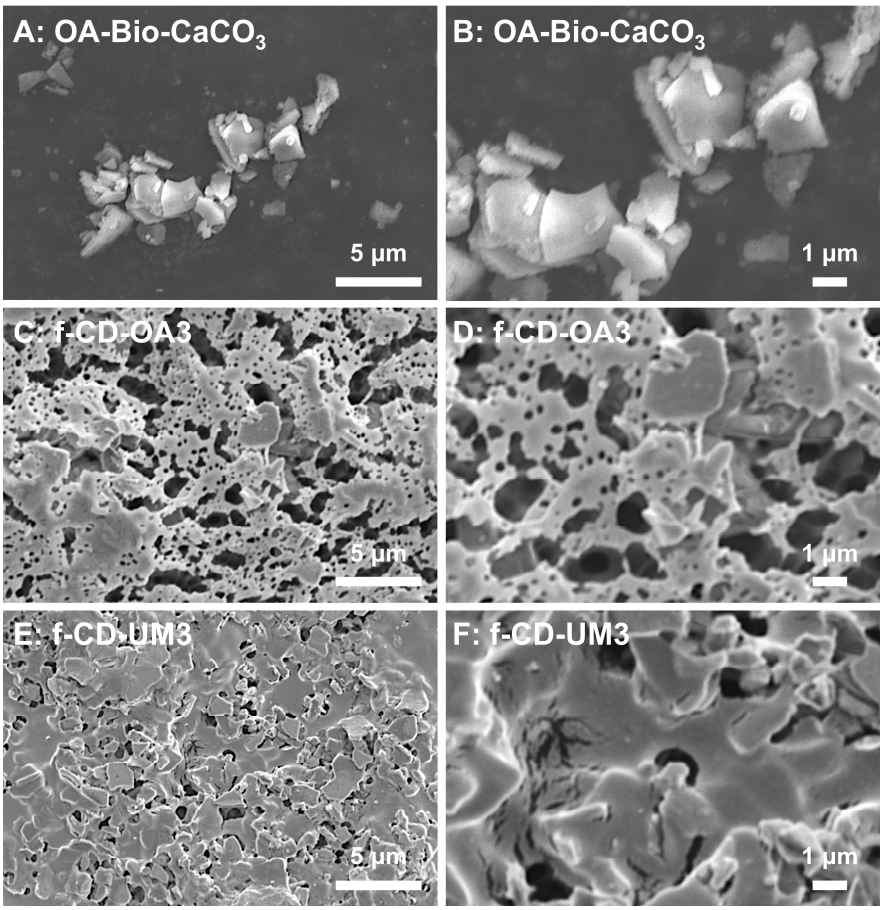


Figure 12. FE-SEM micrographs of OA-Bio-$CaCO_3$ (**A**,**B**), the f-CD-OA3 composite film (**C**,**D**), and the f-CD-UM3 composite film (**E**,**F**). The scale bars in (**A**,**C**,**E**) are 5 µm. The scale bars in (**B**,**D**,**F**) are 1 µm.

3.8. Surface Morphology and Elemental Composition of Uncoated and Coated Mandarins

The CD-OA3 coating dispersion, which produced the f-CD-OA3 composite film with the highest apparent water contact angle, was subsequently selected for application to mandarin peel surfaces. Macroscopic imaging and SEM–EDS analysis demonstrated the formation and subsequent removal of the OA-Bio-$CaCO_3$-containing coating from the mandarin surface. The uncoated P-ManOr sample exhibited the characteristic bright-orange appearance of the peel (Figure 13A), while SEM revealed a relatively compact surface with shallow ridges and few particulate deposits (Figure 13D). Following coating application, the OA-ManOr surface became whitish and opaque (Figure 13B), consistent with extensive

coverage by the mineral-containing composite layer. SEM imaging further revealed a dense accumulation of polygonal OA-Bio-$CaCO_3$ particles, including both dispersed particles and agglomerated domains distributed throughout the coating matrix (Figure 13E). The non-uniform distribution of OA-Bio-$CaCO_3$ deposits is likely influenced by the intrinsic roughness and curvature of the mandarin peel, as well as by localized variations in coating thickness during application and drying. Nevertheless, the SEM micrographs confirm that the composite coating adhered to the fruit surface and formed a particulate protective layer.

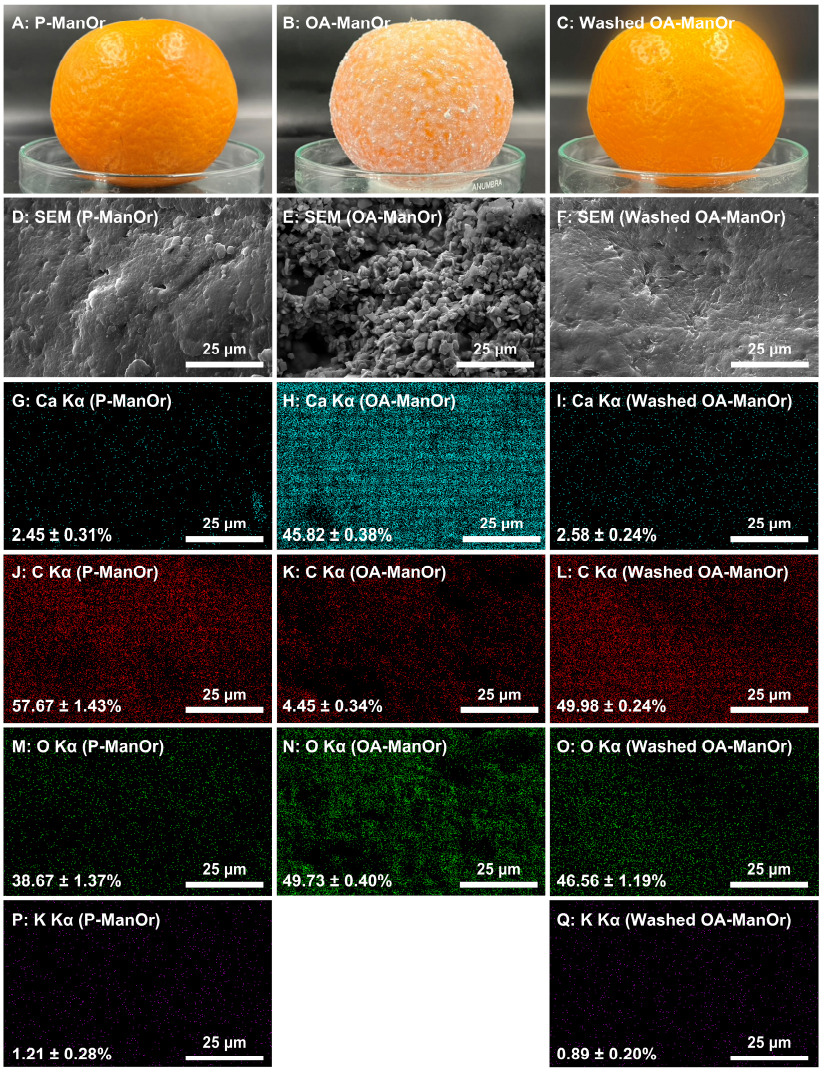


Figure 13. Macroscopic appearance, surface morphology, and elemental distribution of uncoated mandarin (P-ManOr), mandarin coated with the CD-OA3 coating dispersion (OA-ManOr), and OA-ManOr after washing with ultrapure water (Washed OA-ManOr). Photographs of P-ManOr (**A**), OA-ManOr (**B**), and Washed OA-ManOr (**C**); corresponding SEM micrographs (**D**–**F**); EDS elemental maps of Ca Kα (**G**–**I**), C Kα (**J**–**L**), and O Kα (**M**–**O**); and K Kα maps of P-ManOr (**P**) and Washed OA-ManOr (**Q**). The values shown indicate the relative elemental compositions (% (*w*/*w*)) expressed as the mean ± standard deviation. Scale bars = 25 µm.

The elemental maps corroborated the morphological observations. Calcium (Ca), potassium (K), sodium (Na), phosphorus (P), and magnesium (Mg) have been reported as macronutrients naturally present in mandarin peel [1]. Following coating application, the relative Ca content increased markedly from 2.45 ± 0.31% in P-ManOr to 45.82 ± 0.38% in OA-ManOr (Figure 13G,H). The peel of OA-ManOr also exhibited an O content of 49.73 ± 0.40%, whereas the relative C content decreased from 57.67 ± 1.43% to 4.45 ± 0.34%

(Figure 13J,K,M,N). This redistribution in surface elemental composition indicates that the Ca- and O-rich coating phase dominated the EDS sampling volume, thereby attenuating the signal originating from the carbon-rich native peel. Consistent with this interpretation, the absence of a detectable K contribution from OA-ManOr, compared with 1.21 ± 0.28% for P-ManOr, suggests that the composite coating effectively masked the underlying peel surface.

Washing largely restored the original orange appearance of OA-ManOr (Figure 13C). Correspondingly, the dense particulate layer observed before washing was no longer evident, and no residual polygonal OA-Bio-$CaCO_3$ particles were observed on the washed peel surface. The washed surface displayed a morphology resembling that of P-ManOr (Figure 13F). The Ca content decreased to 2.58 ± 0.24%, approaching that of the uncoated surface, while C and O accounted for 49.98 ± 0.24% and 46.56 ± 1.19%, respectively (Figure 13I,L,O). The reappearance of a detectable K signal at 0.89 ± 0.20% further indicated re-exposure of the native peel following coating removal (Figure 13Q). Although the relative C and O contents did not return completely to their initial values, likely because of the natural spatial heterogeneity of the peel, their combined contents were comparable between P-ManOr and Washed OA-ManOr, at 96.34% and 96.54%, respectively.

These findings confirm that the coating formed an extensive OA-Bio-$CaCO_3$-rich particulate barrier on the mandarin surface while remaining substantially removable by washing. Its rough, particle-rich architecture, combined with the hydrophobicity imparted by OA functionalization, may reduce direct contact between pesticide droplets and the native mandarin peel. The marked decrease in surface Ca after washing further supports the intended use of the coating as a temporary protective layer that can be removed before consumption. Nevertheless, the results do not confirm the complete absence of residual particles below the spatial and analytical detection limits of SEM–EDS.

Food-grade forms of $CaCO_3$ have established uses as a food additive and calcium-fortification ingredient, whereas HPMC and OA have been incorporated into edible films and food-coating formulations [128,129]. Nevertheless, these established uses do not necessarily establish the safety or regulatory compliance of OA-Bio-$CaCO_3$ particles or the complete coating formulation. Moreover, because the migration of particles or other coating components into the peel and edible pulp was not directly quantified in this proof-of-concept study, the findings should not be interpreted as evidence that migration did not occur or as a comprehensive assessment of consumer safety. Before practical or commercial implementation, validated migration studies, standardized assessments of residues remaining after washing, comprehensive toxicological evaluations, and confirmation of compliance with the applicable regulations in the intended market will be required. Moreover, the conspicuous whitening caused by the OA-Bio-$CaCO_3$-rich layer may adversely affect the commercial appearance and consumer acceptability of the coated fruit. Therefore, as a precautionary measure, the coating should be regarded as a temporary protective layer and thoroughly removed by washing before marketing and before the fruit is peeled or consumed.

3.9. Preliminary Evaluation of the Developed Hydrophobic Coatings for Reducing Organophosphate Pesticide Deposition

The protective performance of the developed hydrophobic CD-OA3 coating against pesticide deposition on mandarin surfaces was preliminarily evaluated using a colorimetric pesticide-residue test kit (Figure 14). Profenofos residues have been detected in mandarins and other citrus fruits, with monitoring data indicating that profenofos became an increasingly important residue-related risk factor in mandarin and orange samples after 2016 [16]. Notably, the “GT” Test Kit employed in this study responds to organophosphate and carbamate pesticides and other cholinesterase inhibitors. Within the cypermethrin-profenofos formulation used here, profenofos was therefore the analytically relevant active ingredient.

At a pesticide-to-water ratio of 3.0:100 (v/v), the Prof20x_P-ManOr1 sample produced a darker color than the control reference solution, indicating the presence of detectable pesticide residues at an unsafe level on the fruit surface (Figure 14A). A similar response was observed for the Prof20x_UM-ManOr1 sample. In contrast, the Prof20x_OA-ManOr1 sample exhibited a color comparable to or lighter than that of the control reference solution. This result indicates that organophosphate pesticide residues were not detected under the screening conditions and demonstrates the improved protective effect of the coating containing OA-Bio-$CaCO_3$. The superior performance of the CD-OA3 coating is consistent with the enhanced water-repellent properties of the f-CD-OA3 composite film. OA modification introduces hydrophobic hydrocarbon chains onto the Bio-$CaCO_3$ (Sif) surface, thereby reducing the affinity of the coating for aqueous pesticide droplets. The porous and heterogeneous morphology of the composite film observed on OA-ManOr (Figure 13E) may also contribute to its protective performance by decreasing the effective solid–liquid contact area and limiting pesticide-droplet spreading. By comparison, the coating containing Bio-$CaCO_3$ (Sif) exhibited lower water repellency and did not prevent detectable pesticide deposition.

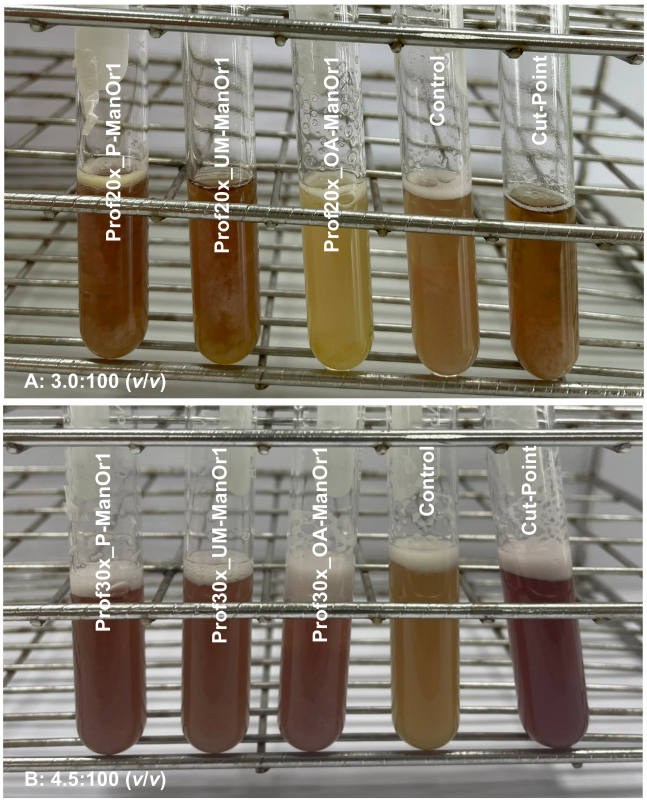


Figure 14. Colorimetric screening of organophosphate pesticide residues on uncoated mandarins (Prof20x_P-ManOr1 and Prof30x_P-ManOr1), mandarins coated with the CD-UM3 formulation (Prof20x_UM-ManOr1 and Prof30x_UM-ManOr1), and mandarins coated with the CD-OA3 formulation (Prof20x_OA-ManOr1 and Prof30x_OA-ManOr1) after exposure to a cypermethrin-profenofos formulation at a formulation-to-water ratio of 3.0:100 (v/v) (**A**) and 4.5:100 (v/v) (**B**). The color responses of the sample tubes were visually compared with those of the control and cut-point reference solutions to assess the presence and relative severity of the pesticide residues.

When the pesticide-to-water ratio was increased to 4.5:100 (v/v), all three mandarin samples, including Prof30x_P-ManOr1, Prof30x_OA-ManOr1, and Prof30x_UM-ManOr1, produced color responses that were darker than the control reference solution and comparable to the cut-point reference solution (Figure 14B). These findings indicate that pesticide

residues were detectable at an unsafe level on the uncoated fruit and on the mandarins coated with either the CD-OA3 or CD-UM3 formulation. The increased pesticide concentration at 30 times the recommended application rate therefore reduced the protective effectiveness of the developed coatings. The colorimetric screening results demonstrated that the CD-OA3 coating reduced pesticide deposition on mandarin surfaces when the cypermethrin-profenofos formulation was applied at up to 20 times the recommended rate. However, its protective effect decreased when the pesticide concentration exceeded this level. Because the GT Test Kit provides a visual screening result rather than a quantitative measurement of individual active ingredients, confirmatory analysis using a chromatographic method, such as gas chromatography–tandem mass spectrometry or liquid chromatography–tandem mass spectrometry, would be beneficial to accurately quantify individual residue concentrations and deposition reductions.

3.10. Quantitative Evaluation of the Developed Hydrophobic Coatings for Reducing the Deposition of Systemic and Non-Systemic Pesticides

To provide a more comprehensive assessment of the efficacy of the CD-OA3 coating in reducing pesticide deposition on mandarin surfaces, acetamiprid and chlorothalonil were selected as representative pesticides with contrasting physicochemical properties and systemic behaviors. Acetamiprid is a systemic, hydrophilic insecticide, whereas chlorothalonil is a non-systemic, contact-active, and lipophilic fungicide. Figure 15 compares the macroscopic appearances of uncoated and CD-OA3-coated mandarins with and without pesticide application. The pesticide-free P-ManOr controls retained their characteristic orange color and surface texture after 1 and 7 d of storage (Figure 15A,B). Similarly, Acet_P-ManOr1 and Acet_P-ManOr7 samples exhibited no pronounced changes in peel appearance over the same period (Figure 15C,D). Ctnl_P-ManOr1 and Ctnl_P-ManOr7 samples also largely retained their original appearance, although slight surface discoloration and isolated dark spots were visible after 7 d (Figure 15E,F). These observations indicate that pesticide application did not cause extensive macroscopic alteration of the uncoated mandarin surfaces under the experimental conditions.

In contrast, OA-ManOr samples exhibited a readily distinguishable whitish particulate layer attributable to the OA-Bio-$CaCO_3$-containing composite coating (Figure 15G,H). This layer remained clearly visible after 7 d of storage, indicating that the coating persisted on the fruit surface throughout the evaluation period. The coating was also retained following the application of acetamiprid and chlorothalonil (Figure 15I–L). No substantial macroscopic disruption or complete detachment of the coating was evident during storage. The continued presence of the coating is consistent with its function as a temporary physical barrier separating pesticide droplets from the native peel surface.

Figure 16 compares the macroscopic appearances of OA-ManOr samples before and after simulated rainfall exposure. Before simulated rainfall exposure, the mandarin surfaces were extensively covered by a readily visible, whitish particulate layer attributable to the OA-Bio-$CaCO_3$-containing CD-OA3 formulation (Figure 16A). Although the coating was distributed heterogeneously, it covered most of the native orange peel. Following simulated rainfall exposure, subsequent pesticide application, and 1 d of storage, a greater proportion of the orange peel became visible, while irregular whitish patches and particulate deposits remained on the fruit surfaces (Figure 16B). These changes indicate partial erosion and redistribution of the coating rather than its complete removal. Despite the apparent reduction in surface coverage, clearly visible residual coating remained on both Acet_SR_OA-ManOr1 and Ctnl_SR_OA-ManOr1 after simulated rainfall exposure and pesticide application.

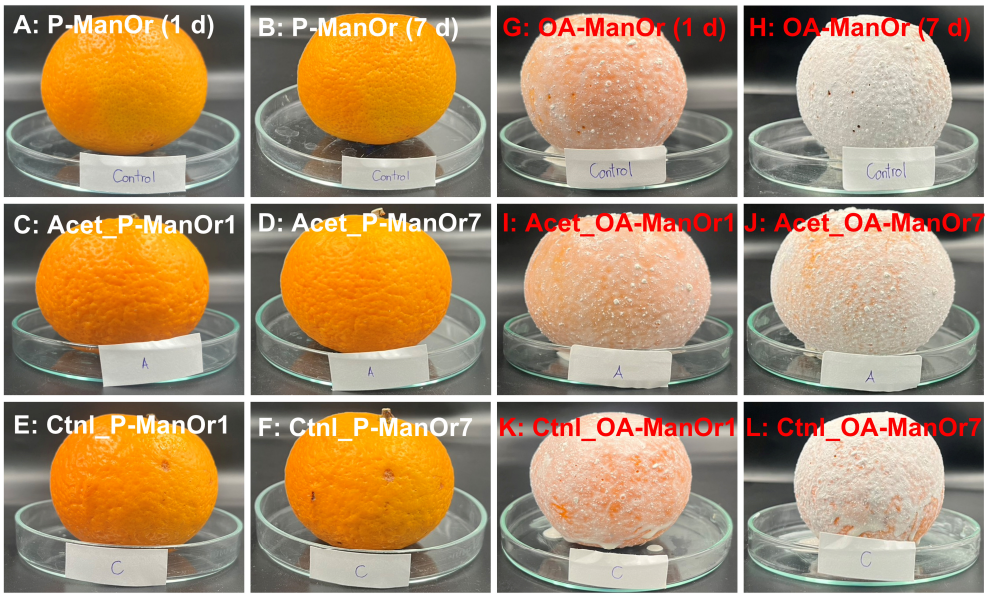


Figure 15. Representative macroscopic appearances of uncoated mandarins (P-ManOr) and mandarins coated with the CD-OA3 formulation (OA-ManOr) after 1 d and 7 d of storage, with or without pesticide application: pesticide-free P-ManOr controls stored for 1 d (**A**) and 7 d (**B**); Acet_P-ManOr1 (**C**); Acet_P-ManOr7 (**D**); Ctnl_P-ManOr1 (**E**); Ctnl_P-ManOr7 (**F**); pesticide-free OA-ManOr controls stored for 1 d (**G**) and 7 d (**H**); Acet_OA-ManOr1 (**I**); Acet_OA-ManOr7 (**J**); Ctnl_OA-ManOr1 (**K**); and Ctnl_OA-ManOr7 (**L**).

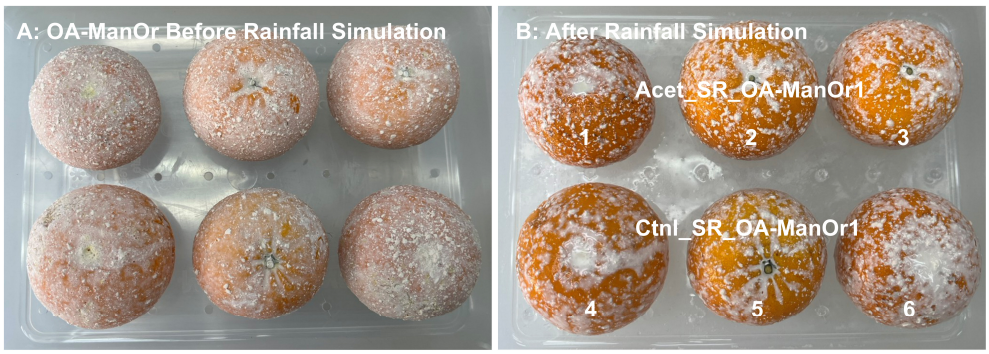


Figure 16. Representative macroscopic appearances of mandarins coated with the CD-OA3 formulation (OA-ManOr) before simulated rainfall exposure (**A**) and following simulated rainfall exposure, subsequent pesticide application, and 1 d of storage (**B**). In panel (**B**), the upper row presents acetamiprid-treated samples (Acet_SR_OA-ManOr1; samples 1–3), whereas the lower row presents chlorothalonil-treated samples (Ctnl_SR_OA-ManOr1; samples 4–6).

The efficacy of the CD-OA3 coating in reducing acetamiprid and chlorothalonil deposition on mandarin surfaces is presented in Figure 17. One day after pesticide application, Acet_OA-ManOr1 exhibited an acetamiprid-deposition reduction of 89 ± 2% relative to the corresponding Acet_P-ManOr1 control. However, the reduction decreased to approximately 22 ± 5% after 7 d relative to the corresponding Acet_P-ManOr7 control and was significantly lower than that observed after 1 d ($p < 0.05$). The time-dependent decline may partly reflect the high aqueous solubility and plant-tissue mobility of acetamiprid, which could facilitate its gradual redistribution from the coating–peel interface into the fruit [130,131]. Additionally, differential dissipation between coated and uncoated fruit may also have contributed to the observed decline [132]. The observed decline should not be attributed exclusively to deterioration of the coating.

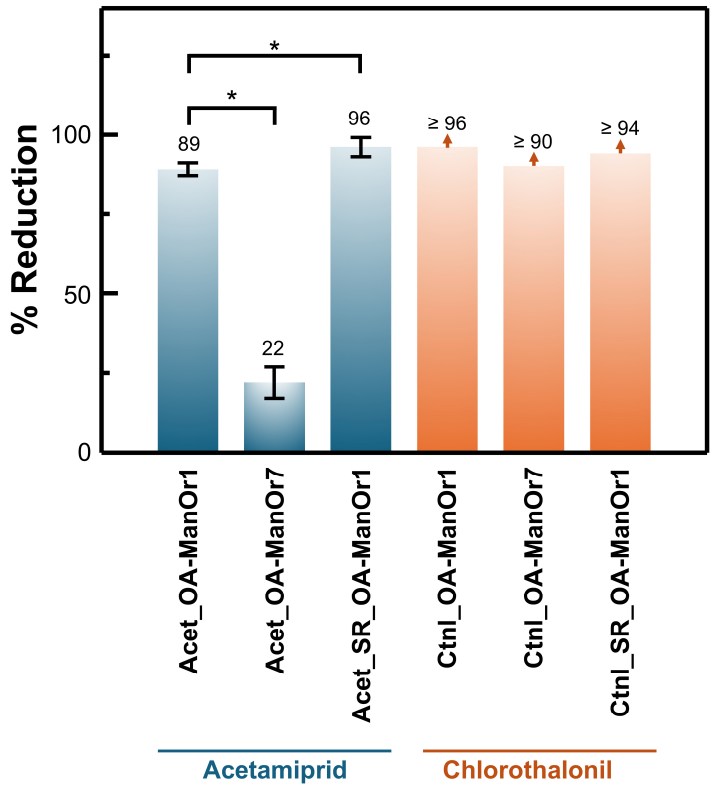


Figure 17. Reduction in acetamiprid and chlorothalonil deposition on mandarins coated with the CD-OA3 formulation, relative to the corresponding uncoated Acet_P-ManOr1, Acet_P-ManOr7, Ctnl_P-ManOr1, or Ctnl_P-ManOr7 controls. Acet_P-ManOr1, Acet_OA-ManOr1, Ctnl_P-ManOr1, and Ctnl_OA-ManOr1 were analyzed 1 d after pesticide application. Acet_SR_OA-ManOr1 and Ctnl_SR_OA-ManOr1 were exposed to simulated rainfall before pesticide application and analyzed after 1 d. Acet_P-ManOr7, Acet_OA-ManOr7, Ctnl_P-ManOr7, and Ctnl_OA-ManOr7 were analyzed 7 d after pesticide application. Acetamiprid results are presented as the mean ± standard deviation (n = 3). Chlorothalonil residues in the coated samples were below the analytical detection limit; therefore, the displayed values represent minimum reduction estimates, as indicated by upward arrows. Asterisks indicate significant differences between the bracketed groups ($p < 0.05$; two-sided independent-samples t-test).

Following simulated rainfall exposure, Acet_SR_OA-ManOr1 exhibited a 96 ± 3% reduction in acetamiprid deposition, which was significantly greater than the reduction observed for Acet_OA-ManOr1 without simulated rainfall treatment after 1 d ($p < 0.05$). These findings demonstrate that the simulated rainfall treatment did not impair the short-term protective performance of the coating. The slightly higher apparent reduction observed after simulated rainfall may possibly reflect water-induced modification of the coating surface. Specifically, rainfall could have preferentially leached or partially dissolved water-accessible HPMC- and glycerol-rich domains and altered the size distribution or spatial organization of the retained OA-Bio-$CaCO_3$ particles, thereby modifying the surface roughness and wettability [133–135]. However, this possibility should not be interpreted as evidence that rainfall intrinsically enhances coating performance.

The CD-OA3 coating exhibited consistently high effectiveness against chlorothalonil deposition. Because chlorothalonil residues in the Ctnl_OA-ManOr1, Ctnl_OA-ManOr7, and Ctnl_SR_OA-ManOr1 samples were below the analytical detection limit of 0.005 mg/kg, the corresponding values represent minimum rather than exact reductions. Consequently, statistical differences among the chlorothalonil treatments were not evaluated. The calculated lower-bound reductions were ≥96% for the Ctnl_OA-ManOr1 sample, ≥90% for the Ctnl_OA-ManOr7 sample, and ≥94% for the Ctnl_SR_OA-ManOr1 sample following simu-

lated rainfall. The sustained apparent reduction in chlorothalonil deposition may reflect its predominantly surface-localized behavior [136]. As a non-systemic contact fungicide, chlorothalonil exhibits limited translocation into plant tissues, favoring its retention on the composite coating or fruit surfaces through hydrophobic interactions [137]. The removable composite coating may therefore function as a temporary sacrificial barrier that limits direct pesticide–peel contact and facilitates the removal of deposited chlorothalonil together with the coating layer.

These findings demonstrate that the protective performance of the CD-OA3 coating was pesticide-dependent. Its visible persistence on the mandarin surface was consistent with the observed reductions in pesticide deposition. The coating provided substantial short-term protection against acetamiprid deposition, although its relative effectiveness declined during storage. In contrast, consistently high minimum reduction estimates were obtained for chlorothalonil after both storage and simulated rainfall exposure. Despite the partial loss and redistribution of the coating following simulated rainfall, the remaining surface coverage maintained reductions of approximately 96% for acetamiprid and at least 94% for chlorothalonil. These results indicate that complete macroscopic coverage was not required to retain substantial protective efficacy under the simulated rainfall conditions employed. The contrasting responses to the two pesticides highlight the importance of considering compound-specific physicochemical properties and systemic behavior when evaluating the performance of protective coatings on mandarin surfaces. Further studies encompassing a broader range of rainfall intensities, durations, and repeated exposure events are required to establish the durability and protective performance of the coating under field-relevant environmental conditions.

4. Conclusions

This study demonstrated the successful recovery of biogenic calcium carbonate (Bio-$CaCO_3$) from Asian green mussel (*Perna viridis*) shell waste through combined chemical treatment and mechanical pulverization. The refined and sieved Bio-$CaCO_3$ [Bio-$CaCO_3$ (Sif)] exhibited the aragonite polymorph and a polygonal, plate-like morphology, with a volume-based mean diameter and a mean particle length of 34.47 ± 2.29 and 2.55 ± 0.72 μm, respectively, and a high specific surface area of 922.73 ± 4.88 m^2/kg. At the optimal oleic acid (OA) concentration, the OA-functionalized Bio-$CaCO_3$ (Sif) (OA-Bio-$CaCO_3$) powder beds displayed apparent superhydrophobicity, with a water contact angle of $152.7° \pm 2.7°$. ATR FT-IR and X-ray photoelectron spectroscopic analyses supported the successful functionalization of the Bio-$CaCO_3$ (Sif) surface with OA. Incorporation of OA-Bio-$CaCO_3$ into the HPMC-glycerol (Gro) matrix produced an optimized hydrophobic composite film with an initial apparent water contact angle of $92.5° \pm 9.6°$, which retained its water-repellent properties after continuous contact with a water droplet for 10 min. The optimized HPMC-Gro-OA-Bio-$CaCO_3$ formulation was successfully applied to mandarin surfaces by dip-coating. Colorimetric screening indicated that the coating limited organophosphate pesticide deposition on mandarin surfaces even when the pesticide was applied at up to 20 times the label-recommended rate. Relative to uncoated controls, quantitative residue analyses showed reductions of 89% and ≥96% in acetamiprid and chlorothalonil deposition, respectively, after 1 d of storage. After 7 d of storage, the protective efficacy of the developed hydrophobic coating was pesticide-dependent: the reduction in chlorothalonil deposition remained at least of 90%, whereas the reduction in acetamiprid deposition declined to 22 ± 5%. Following simulated rainfall exposure, the reductions in acetamiprid and chlorothalonil deposition were 96% and ≥94%, respectively. This study demonstrates that an HPMC-Gro coating containing oleic-acid-functionalized, mussel-shell-derived Bio-$CaCO_3$ can reduce pesticide deposition on mandarin surfaces, supported by colorimetric

screening of a profenofos-containing formulation and quantitative analyses of acetamiprid and chlorothalonil. Furthermore, this study demonstrates a promising strategy for valorizing Asian green mussel shell waste through its application as a functional agricultural coating material for reducing pesticide deposition on fresh fruits and supporting more sustainable agricultural practices and potential food-safety applications. Further field-scale studies addressing coating durability, repeated rainfall exposure, component migration, removal by washing, consumer safety, and regulatory compliance are required before practical application.

Author Contributions: Conceptualization, S.E. and T.P.; methodology, S.E. and C.L.; investigation, S.M., S.K., S.J. and T.P.; resources, S.E. and C.L.; data curation, S.M., S.K., S.J. and T.P.; writing—original draft preparation, T.P.; writing—review and editing, T.P.; supervision, T.P.; project administration, T.P.; funding acquisition, T.P. All authors have read and agreed to the published version of the manuscript.

Funding: This research was funded by King Mongkut's University of Technology North Bangkok under Contract No. KMUTNB-FF-68-B-68.

Data Availability Statement: The original contributions presented in this study are included in the article. Further inquiries can be directed to the corresponding author.

Acknowledgments: The authors gratefully acknowledge research support from the Department of Industrial Chemistry, Faculty of Applied Science, King Mongkut's University of Technology North Bangkok, and the Sensor Research Unit (SRU), Department of Chemistry, Faculty of Science, Chulalongkorn University.

Conflicts of Interest: The authors declare no conflicts of interest.

Abbreviations

The following abbreviations are used in this manuscript:

Bio-$CaCO_3$	Biogenic calcium carbonate derived from Asian green mussel shell waste
OA-Bio-$CaCO_3$	Oleic acid-functionalized biogenic calcium carbonate
OA	Oleic acid
HPMC	Hydroxypropyl methylcellulose
Gro	Glycerol
FE-SEM	Field-emission scanning electron microscopy
ATR FT-IR	Attenuated total reflectance Fourier-transform infrared spectroscopy
XPS	X-ray photoelectron spectroscopy

References

1. Czech, A.; Zarycka, E.; Yanovych, D.; Zasadna, Z.; Grzegorczyk, I.; Kłys, S. Mineral Content of the Pulp and Peel of Various Citrus Fruit Cultivars. *Biol. Trace Elem. Res.* **2020**, *193*, 555–563. [CrossRef] [PubMed]
2. Garg, R.; Anjum, A.; Garg, R.; Eddy, N.O.; Watandost, H. Citrus fruits as sources of bioactive compounds for multifaceted applications. *Discov. Food* **2026**, *6*, 152. [CrossRef]
3. Shorbagi, M.; Fayek, N.M.; Shao, P.; Farag, M.A. Citrus reticulata Blanco (the common mandarin) fruit: An updated review of its bioactive, extraction types, food quality, therapeutic merits, and bio-waste valorization practices to maximize its economic value. *Food Biosci.* **2022**, *47*, 101699. [CrossRef]
4. Khaleel, G.; Sharanagat, V.S.; Singh, L.; Kumar, Y.; Kumar, K.; Kishore, A.; Saikumar, A.; Mani, S. Characterization of kinnow (citrus reticulate) peel and its effect on the quality of muffin. *J. Food Process. Preserv.* **2022**, *46*, e16716. [CrossRef]
5. Durmus, N.; Gulsunoglu-Konuskan, Z.; Kilic-Akyilmaz, M. Recovery, Bioactivity, and Utilization of Bioactive Phenolic Compounds in Citrus Peel. *Food Sci. Nutr.* **2024**, *12*, 9974–9997. [CrossRef] [PubMed]
6. Rashid, R.; Wani, S.M.; Manzoor, S.; Masoodi, F.A.; Dar, M.M. Improving oxidative stability of edible oils with nanoencapsulated orange peel extract powder during accelerated shelf life storage. *Food Biosci.* **2022**, *49*, 101917. [CrossRef]
7. Cho, Y.; Hwang, S.; Ninh, P.T.T.; Kim, Y.; Choe, S.; Myung, J. Sustainable valorization of mandarin peel waste into multifunctional cellulose/pectin/PVA films with superior mechanical and UV-blocking performance. *RSC Sustain.* **2026**, *4*, 289–303. [CrossRef]

8. Zhang, G.; Mak, H.; Zhang, Z.; Zhang, T.; Wang, Y.; Zhang, R.-Y.; Liu, H.-M.; Zhou, S.; Wu, B. Fully unlocking the potential of Chenpi (Citri Reticulatae Pericarpium) as a functional ingredient in food development. *Sustain. Food Technol.* **2026**, *4*, 3399–3412. [CrossRef]
9. Liu, H.; Wen, J.; Xu, Y.; Wu, J.; Yu, Y.; Yang, J.; Liu, H.; Fu, M. Evaluation of dynamic changes and formation regularity in volatile flavor compounds in Citrus reticulata 'chachi' peel at different collection periods using gas chromatography-ion mobility spectrometry. *LWT* **2022**, *171*, 114126. [CrossRef]
10. Deng, H.; Zhang, Y.; Reuss, L.; Suh, J.H.; Yu, Q.; Liang, G.; Wang, Y.; Gmitter, F.G., Jr. Comparative Leaf Volatile Profiles of Two Contrasting Mandarin Cultivars against Candidatus Liberibacter asiaticus Infection Illustrate Huanglongbing Tolerance Mechanisms. *J. Agric. Food Chem.* **2021**, *69*, 10869–10884. [CrossRef] [PubMed]
11. Noorizadeh, S.; Golmohammadi, M.; Bagheri, A.; Bertaccini, A. Citrus industry: Phytoplasma-associated diseases and related challenges for Asia, America and Africa. *Crop Prot.* **2022**, *151*, 105822. [CrossRef]
12. Meena, P.N.; Raghavendra, D.; Singh, S.; Kumar, N.; Khokhar, M.K.; Chander, S.; Lal, M.K.; Tiwari, R.K.; Kumar, R. Integrated Pest Management techniques in a Kinnow mandarin (Citrus reticulata Blanco) orchard with an emphasis on yield improvement. *Heliyon* **2025**, *11*, e42574. [CrossRef] [PubMed]
13. Xiao, Z.; Yang, C.; Wei, Z.; Fu, X.; Zhao, C.; Li, G. A spectral-physiological feature fusion model for the early detection of anthracnose in citrus leaves. *Comput. Electron. Agric.* **2026**, *243*, 111410. [CrossRef]
14. Bibi, A.; Rafique, N.; Khalid, S.; Samad, A.; Ahad, K.; Mehboob, F. Method optimization and validation for the routine analysis of multi-class pesticide residues in Kinnow Mandarin and fruit quality evaluation. *Food Chem.* **2022**, *369*, 130914. [CrossRef] [PubMed]
15. Al-Nasir, F.M.; Jiries, A.G.; Al-Rabadi, G.J.; Alu'datt, M.H.; Tranchant, C.C.; Al-Dalain, S.A.; Alrabadi, N.; Madanat, O.Y.; Al-Dmour, R.S. Determination of pesticide residues in selected citrus fruits and vegetables cultivated in the Jordan Valley. *LWT* **2020**, *123*, 109005. [CrossRef]
16. Li, Z.; Zhang, Y.; Zhao, Q.; Wang, C.; Cui, Y.; Li, J.; Chen, A.; Liang, G.; Jiao, B. Occurrence, temporal variation, quality and safety assessment of pesticide residues on citrus fruits in China. *Chemosphere* **2020**, *258*, 127381. [CrossRef] [PubMed]
17. Ar Reshaid, A.; Alshemaimri, D.; Khabbouchi, M.; Alhotan, A.; Almutairi, S.; Aljarbou, W. Pesticide residues in fruits from Riyadh markets: A three-year evaluation. *Environ. Monit. Assess.* **2025**, *197*, 1253. [CrossRef] [PubMed]
18. Malhat, F.; Abdel-Megeed, M.; Saber, E.-S.; Shokr, S.A.S.; Eissa, F. Pesticide residues in fruits from Egyptian markets: Detection, compliance, co-occurrence, and health risk assessment. *J. Food Compos. Anal.* **2025**, *145*, 107842. [CrossRef]
19. Alenazi, M.; Al-Zaid, A.; Najai, J.; Al-Dossari, A.; Al-Batti, A.; Al-Bahouth, F. Pesticide residue distribution in citrus fruits: Effectiveness of peeling as a mitigation strategy. *Environ. Pollut. Manag.* **2025**, *2*, 114–121. [CrossRef]
20. Chmielewski, J.; Gworek, B.; Florek-Łuszczki, M.; Górska, E.; Łuszczki, J. Health Dietary Exposure to Pesticide Residues in Citrus Fruits and Bananas: A Screening-Level Risk Assessment Using Official Monitoring Data and EFSA PRIMo Scenarios. *Expo. Health* **2026**, *18*, 31. [CrossRef]
21. European Food Safety Authority; Carrasco Cabrera, L.; Di Piazza, G.; Dujardin, B.; Marchese, E.; Medina Pastor, P. The 2023 European Union report on pesticide residues in food. *EFSA J.* **2025**, *23*, e9398. [CrossRef] [PubMed]
22. Karaağaçlı, H.; Balkan, T.; Kızılarslan, M.; Kara, K. Pesticide residues in citrus fruits from Türkiye: Assessment of distribution, matrix effects, and health risks in lemon, mandarin, and orange. *J. Food Compos. Anal.* **2025**, *147*, 108091. [CrossRef]
23. European Food Safety Authority; Medina Pastor, P.; Carrasco Cabrera, L.; Di Piazza, G.; González Ciria, C. The 2024 European Union report on pesticide residues in food. *EFSA J.* **2026**, *24*, e10054. [CrossRef] [PubMed]
24. Li, Z.; Zhang, Y.; Zhao, Q.; Cui, Y.; He, Y.; Li, J.; Yang, Q.; Lin, Z.; Wang, C.; Liang, G.; et al. Determination, distribution and potential health risk assessment of insecticides and acaricides in citrus fruits of China. *J. Food Compos. Anal.* **2022**, *111*, 104645. [CrossRef]
25. Acoglu, B.; Omeroglu, P.Y. Effectiveness of different type of washing agents on reduction of pesticide residues in orange (*Citrus sinensis*). *LWT* **2021**, *147*, 111690. [CrossRef]
26. Li, M.; Pan, K.; Xin, L.; Wei, S. Advancement and Trends in High-Throughput Analysis of Pesticide Residues in Fruits and Vegetables: A Comprehensive Review. *ACS Agric. Sci. Technol.* **2026**, *6*, 257–277. [CrossRef]
27. Zhou, W.; Arcot, Y.; Medina, R.F.; Bernal, J.; Cisneros-Zevallos, L.; Akbulut, M.E.S. Integrated Pest Management: An Update on the Sustainability Approach to Crop Protection. *ACS Omega* **2024**, *9*, 41130–41147. [CrossRef] [PubMed]
28. Ayodhya, D. Recent advancement in pesticide formulations for pest management and residue analysis by analytical techniques in agriculture using nanocomposites. *Rev. Mater. Res.* **2025**, *1*, 100130. [CrossRef]
29. Chen, Y.; Li, H.; Peng, Y.; Li, T.; Li, X.; Wang, C.; Xiao, R.; Dong, J.; Du, X. Nanoization of Technical Pesticides: Facile and Smart Pesticide Nanocapsules Directly Encapsulated through "On Site" Metal–Polyphenol Coordination Assembly for Improved Efficacy and Biosafety. *J. Agric. Food Chem.* **2025**, *73*, 2865–2879. [CrossRef] [PubMed]
30. Saxena, J. Application of electrolysed water in post-harvest treatment of fruits and vegetables. *Sustain. Food Technol.* **2024**, *2*, 281–291. [CrossRef]

31. Azam, S.M.R.; Ma, H.; Xu, B.; Devi, S.; Siddique, M.A.B.; Stanley, S.L.; Bhandari, B.; Zhu, J. Efficacy of ultrasound treatment in the removal of pesticide residues from fresh vegetables: A review. *Trends Food Sci. Technol.* **2020**, *97*, 417–432. [CrossRef]
32. Fernandes, F.A.N.; Rodrigues, S. Cold plasma technology for sustainable food production: Meeting the United Nations sustainable development goals. *Sustain. Food Technol.* **2025**, *3*, 32–53. [CrossRef]
33. Baswal, A.K.; Dhaliwal, H.S.; Singh, Z.; Mahajan, B.V.C.; Kalia, A.; Gill, K.S. Influence of carboxy methylcellulose, chitosan and beeswax coatings on cold storage life and quality of Kinnow mandarin fruit. *Sci. Hortic.* **2020**, *260*, 108887. [CrossRef]
34. Cao, S.; Liu, M.; Zou, L.; He, Y.; Ren, D.; Wu, X.; Xu, D. Addition of montmorillonite to improve the barrier and wetting properties of chitosan-based coatings and the application on the preservation of Shatang mandarin. *Food Packag. Shelf Life* **2022**, *33*, 100889. [CrossRef]
35. Jurić, S.; Bureš, M.S.; Vlahoviček-Kahlina, K.; Stracenski, K.S.; Fruk, G.; Jalšenjak, N.; Bandić, L.M. Chitosan-based layer-by-layer edible coatings application for the preservation of mandarin fruit bioactive compounds and organic acids. *Food Chem. X* **2023**, *17*, 100575. [CrossRef] [PubMed]
36. Kaur, M.; Gupta, N.; Jawandha, S.K.; Gill, P.S.; Grewal, S.K. Effects of Composite Coating of Aloe vera and Neem Leaf Extract on Storage of 'Kinnow'. *Appl. Fruit Sci.* **2025**, *67*, 266. [CrossRef]
37. Ma, P.; Jia, X.; Zhang, X.; Li, Y.; He, Y.; Li, T.; Wu, C.; Joo, Y.H.; Lee, S.-H.; Meng, T.; et al. Ion-chelated porous chitosan nanocrystal for highly efficient postharvest preservation. *Matter* **2024**, *7*, 2567–2580. [CrossRef]
38. Jin, T.; Wan, Z.; Chiu, I.; Yan, S.; Wijaya, G.O.; Rojas, O.; Chou, K.C.; Yada, R.Y.; Yang, T. Dual-Function Metal–Phenolic Network-Capped Starch Nanoparticles for Postharvest Pesticide Removal and Produce Preservation. *ACS Nano* **2026**, *20*, 12268–12284. [CrossRef] [PubMed]
39. Singh, D.P.; Babukuttan Sheela, U.; Packirisamy, G. Eco-Friendly Plant Polysaccharide-Based Sustainable Coating for Extension of Shelf Life and Removal of Pesticides in Horticulture Produce. *ACS Appl. Bio Mater.* **2025**, *8*, 1559–1570. [CrossRef] [PubMed]
40. Sousa, F.F.; Pinsetta Junior, J.S.; Oliveira, K.T.E.F.; Rodrigues, E.C.N.; Andrade, J.P.; Mattiuz, B.-H. Conservation of 'Palmer' mango with an edible coating of hydroxypropyl methylcellulose and beeswax. *Food Chem.* **2021**, *346*, 128925. [CrossRef] [PubMed]
41. Alemu, T.T.; Intipunya, P.; Gebeyo, B.A. A comprehensive review of edible coatings for postharvest management of fruits and vegetables: Enhancing food and nutrition security. *Discov. Agric.* **2025**, *3*, 190. [CrossRef]
42. Muna, A.; Aflaha, R.; Salsabila, S.; Rusliman, D.; Triyana, K.; Rianjanu, A.; Wibowo, C.; Wasisto, H.S. Polysaccharide-based layer-by-layer edible coatings for shelf-life extension of fresh tomatoes. *Sustain. Food Technol.* **2026**, *4*, 1714–1727. [CrossRef]
43. European Food Safety Authroity; Alvarez, F.; Anastassiadou, M.; Arena, M.; Auteri, D.; Brancato, A.; Bura, L.; Carrasco Cabrera, L.; Castoldi, A.F.; Chaideftou, E.; et al. Peer review of the pesticide risk assessment of the active substance calcium carbonate. *EFSA J.* **2021**, *19*, e06500. [CrossRef] [PubMed]
44. Gullo, G.; Dattola, A.; Vonella, V.; Zappia, R. Effects of two reflective materials on gas exchange, yield, and fruit quality of sweet orange tree *Citrus sinensis* (L.) Osb. *Eur. J. Agron.* **2020**, *118*, 126071. [CrossRef]
45. Teixeira, G.C.M.; Junior, J.S.P.; Mattiuz, B.-H.; Prado, R.d.M.; Corrêa, A.J.; Rocha, A.M.S.; do Vale, D.W. Spraying of calcium carbonate nanoparticles on pineapple fruit reduces sunburn damage. *S. Afr. J. Bot.* **2022**, *148*, 643–651. [CrossRef]
46. da Silva, P.S.O.; de Oliveira, L.F.G.; de Mattos, E.C.; dos Santos Maciel, L.B.; dos Santos, M.P.F.; de Oliveira Alves Sena, E.; Borges Barbosa, N.T.; Gutierrez Carnelossi, M.A.; Fagundes, J.L. Calcium particle films promote artificial shading and photoprotection in leaves of American grapevines (*Vitis labrusca* L.). *Sci. Hortic.* **2019**, *252*, 77–84. [CrossRef]
47. Oliveira da Silva, P.S.; de Oliveira Alves Sena, E.; Silva Gonzaga, M.I.; Ganassali de Oliveira, L.F.; dos Santos Maciel, L.B.; Pinheiro Fiaes dos Santos, M.; Costa de Mattos, E.; Lima Dias, K.L.; Botelho Carneiro, R.; Gutierrez Carnelossi, M.A. Calcium carbonate particle films and water regimes affect the acclimatization, ecophysiology and reproduction of tomato. *Environ. Exp. Bot.* **2019**, *165*, 19–29. [CrossRef]
48. da Silva, P.S.O.; Oliveira, L.F.G.; Silva Gonzaga, M.I.; de Oliveira Alves Sena, E.; dos Santos Maciel, L.B.; Pinheiro Fiaes, M.; de Mattos, E.C.; Gutierrez Carnelossi, M.A. Effects of calcium particle films and natural shading on ecophysiological parameters of conilon coffee. *Sci. Hortic.* **2019**, *245*, 171–177. [CrossRef]
49. Irfa'i, M.A.; Schmahl, W.W.; Pusparizkita, Y.M.; Muryanto, S.; Prihanto, A.; Ismail, R.; Jamari, J.; Bayuseno, A.P. Hydrothermally synthesized-nanoscale carbonated hydroxyapatite with calcium carbonates derived from green mussel shell wastes. *J. Mol. Struct.* **2024**, *1306*, 137837. [CrossRef]
50. Azarian, M.H.; Sutapun, W. Biogenic calcium carbonate derived from waste shells for advanced material applications: A review. *Front. Mater.* **2022**, *9*, 1024977. [CrossRef]
51. Alonso, A.A.; Álvarez-Salgado, X.A.; Antelo, L.T. Assessing the impact of bivalve aquaculture on the carbon circular economy. *J. Clean. Prod.* **2021**, *279*, 123873. [CrossRef]
52. Seesanong, S.; Seangarun, C.; Boonchom, B.; Phutphat, S.; Rungrojchaipon, P.; Montri, N.; Thompho, S.; Boonmee, W.; Laohavisuti, N. Efficient, Green, and Low-Cost Conversion of Bivalve-Shell Wastes to Value-Added Calcium Lactate. *ACS Omega* **2023**, *8*, 27044–27055. [CrossRef] [PubMed]

53. Boudreau, S.; Lam, E.; Kerton, F.M. Accessing biominerals from by-products wasted by the seafood processing industry. *RSC Sustain.* **2026**, *4*, 28–60. [CrossRef]
54. Ismail, R.; Fitriyana, D.F.; Santosa, Y.I.; Nugroho, S.; Hakim, A.J.; Al Mulqi, M.S.; Jamari, J.; Bayuseno, A.P. The potential use of green mussel (*Perna viridis*) shells for synthetic calcium carbonate polymorphs in biomaterials. *J. Cryst. Growth* **2021**, *572*, 126282. [CrossRef]
55. Thongnopkun, P.; Roubroumlert, W.; Lertvachirapaiboon, C. Variable-Sized Green Mussel Shell Waste: Potential Use in Artificial Sand Production. *Sustainability* **2025**, *17*, 7214. [CrossRef]
56. Li, H.-Y.; Tan, Y.-Q.; Zhang, L.; Zhang, Y.-X.; Song, Y.-H.; Ye, Y.; Xia, M.-S. Bio-filler from waste shellfish shell: Preparation, characterization, and its effect on the mechanical properties on polypropylene composites. *J. Hazard. Mater.* **2012**, *217–218*, 256–262. [CrossRef] [PubMed]
57. Murphy, J.N.; Schneider, C.M.; Mailänder, L.K.; Lepillet, Q.; Hawboldt, K.; Kerton, F.M. Wealth from waste: Blue mussels (*Mylitus edulis*) offer up a sustainable source of natural and synthetic nacre. *Green Chem.* **2019**, *21*, 3920–3929. [CrossRef]
58. Kennedy, W.J.; Taylor, J.D.; Hall, A. Environmental and biological controls on bivalve shell mineralogy. *Biol. Rev.* **1969**, *44*, 499–530. [CrossRef] [PubMed]
59. Sarofa, U.; Rosida, D.F.; Khafsa, N. The role of base types and concentration in the deacetylation process of manufacturing chitosan from green mussel shells (*Perna viridis*). *Food Res.* **2025**, *9*, 211–216. [CrossRef] [PubMed]
60. Lertvachirapaiboon, C.; Jirapisitkul, T.; Pienpinijtham, P.; Wongravee, K.; Thammacharoen, C.; Ekgasit, S. Air-gap-enhanced pearlescent effect in periodic stratified bilayers of Perna viridis shell. *J. Mater. Sci.* **2014**, *49*, 6282–6289. [CrossRef]
61. Basay, C.P., Jr.; Patthanavarit, J.; Kaewpraek, N.; Ekgasit, S. Aragonite Calcium Carbonate Microparticles Derived from Asian Green Mussel Shells as Potential Bioinsecticide. *Philipp. J. Sci.* **2025**, *154*, 13–22.
62. González-Chang, M.; Boyer, S.; Creasy, G.L.; Lefort, M.-C.; Wratten, S.D. Mussel shell mulch can increase vineyard sustainability by changing scarab pest behaviour. *Agron. Sustain. Dev.* **2017**, *37*, 42. [CrossRef]
63. Amornkitbamrung, L.; Thanawinitcharoen, A.; Lertvachirapaiboon, C.; Ahn, C.-H.; Ekgasit, S.; Rimdusit, S. Eco-friendly water barrier coating for paper packaging: Harnessing bio-calcium carbonate from mussel shell waste. *Clean. Mater.* **2025**, *16*, 100318. [CrossRef]
64. Nasir, N.A.M.; Kamaruzzaman, W.M.I.W.M.; Badruddin, M.A.; Mohd Ghazali, M.S. Surface modification effects of $CaCO_3$ and TiO_2 nanoparticles in nonpolar solvents. *J. Dispers. Sci. Technol.* **2024**, *45*, 870–879. [CrossRef]
65. Kim, J.; Bea, S.K.; Kim, Y.H.; Kim, D.-W.; Lee, K.-Y.; Lee, C.-M. Improved suspension stability of calcium carbonate nanoparticles by surface modification with oleic acid and phospholipid. *Biotechnol. Bioprocess Eng.* **2015**, *20*, 794–799. [CrossRef]
66. Verma, S.; Chatterjee, S. Biodegradation of profenofos, an acetylcholine esterase inhibitor by a psychrotolerant strain *Rahnella* sp. PFF2 and degradation pathway analysis. *Int. Biodeterior. Biodegrad.* **2021**, *158*, 105169. [CrossRef]
67. Kundu, S.K.; Sayeed, A.; Shanta, S.A.; Tanny, B.R.; Khatun, P.; Kundu, S.R.; Rocky, Z.H.; Maruf, M.A.A.; Bhattacharjee, B.; Basu, T. Effects of Low-Dose Cypermethrin Exposure on the Liver and Kidney of Swiss Albino Mice: Histopathological and Biochemical Insights. *Vet. Med. Sci.* **2026**, *12*, e70706. [CrossRef] [PubMed]
68. Mode of Action Classification Scheme by Insecticide Resistance Action Committee (IRAC) International MoA Working Group. Available online: https://irac-online.org/documents/moa-classification/ (accessed on 9 August 2026).
69. Li, J.; He, B.; Du, G.; Guo, Q.; Bai, C.; Zhang, Y.; Ren, W.; Zhao, W.; Xu, Y. A Multifunctional "Three-in-One" Immunochromatographic Platform Enabled by Honeycomb-Like Trimetallic Mesoporous Nanozymes with Colorimetric, Catalytic, and Fluorescence Activities for Highly Sensitive Acetamiprid Sensing. *Anal. Chem.* **2025**, *97*, 24530–24542. [CrossRef] [PubMed]
70. Wu, T.; Han, B.; Wang, X.; Tong, Y.; Liu, F.; Diao, Q.; Dai, P. Chlorothalonil alters the gut microbiota and reduces the survival of immature honey bees reared in vitro. *Pest Manag. Sci.* **2022**, *78*, 1976–1981. [CrossRef] [PubMed]
71. Fungicide Use in Field Crops Web Book: 1.4: Fungicide Resistance Action Committee (FRAC) Code. Available online: https://cropprotectionnetwork.org/web-books/fungicide-use-in-field-crops?section=14-fungicide-resistance-action-committee-frac-code (accessed on 9 August 2026).
72. de Lima e Silva, C.; de Rooij, W.; Verweij, R.A.; van Gestel, C.A.M. Toxicity in Neonicotinoids to Folsomia candida and Eisenia andrei. *Environ. Toxicol. Chem.* **2020**, *39*, 548–555. [CrossRef] [PubMed]
73. Palladino, C.; Puigvert, F.; Muela, A.; Taborda, B.; Pérez, C.A.; Pérez-Parada, A.; Pareja, L. Evaluation of Fusarium mycotoxins and fungicide residues in barley grain produced in Uruguay. *J. Agric. Food Res.* **2021**, *3*, 100092. [CrossRef]
74. Meng, C.; He, Q.; Huang, J.-W.; Cao, Q.; Yan, X.; Li, S.-P.; Jiang, J.-D. Degradation of chlorothalonil through a hydrolytic dehalogenase secreted from Bacillus subtilis WB800. *Int. Biodeterior. Biodegrad.* **2015**, *104*, 97–104. [CrossRef]
75. Tan, C.; Zhu, G.; Pan, Z.; Tian, M.; Li, X.; Du, S.; Gao, T.; Xue, F. Determination and Correlation of Solubility of Chlorothalonil in 10 Pure Solvents and One Binary Solvent at 288.15–323.15 K. *J. Chem. Eng. Data* **2025**, *70*, 1520–1526. [CrossRef]
76. Lertvachirapaiboon, C.; Parnklang, T.; Pienpinijtham, P.; Wongravee, K.; Thammacharoen, C.; Ekgasit, S. Selective colors reflection from stratified aragonite calcium carbonate plates of mollusk shells. *J. Struct. Biol.* **2015**, *191*, 184–189. [CrossRef] [PubMed]

77. Ehrlich, H.; Martinović, R.; Joksimović, D.; Petrenko, I.; Schiaparelli, S.; Wysokowski, M.; Tsurkan, D.; Stelling, A.L.; Springer, A.; Gelinsky, M.; et al. Conchixes: Organic scaffolds which resemble the size and shapes of mollusks shells, their isolation and potential multifunctional applications. *Appl. Phys. A* **2020**, *126*, 562. [CrossRef]
78. Polat, E.; Güler, T.; Celep, O.; Aktürk, S. Investigation on the production of oleic acid coated calcium carbonate from marble dust by flotation. *Miner. Eng.* **2025**, *232*, 109505. [CrossRef]
79. Hu, Z.; Deng, Y. Superhydrophobic Surface Fabricated from Fatty Acid-Modified Precipitated Calcium Carbonate. *Ind. Eng. Chem. Res.* **2010**, *49*, 5625–5630. [CrossRef]
80. Commission Regulation (EU) 2025/1212 of 24 June 2025 Amending Annex II to Regulation (EC) No 396/2005 of the European Parliament and of the Council as Regards Maximum Residue Levels for Acetamiprid in or on Certain Products. Available online: http://data.europa.eu/eli/reg/2025/1212/oj (accessed on 10 August 2026).
81. Commission Regulation (EU) 2016/67 of 19 January 2016 Amending Annexes II, III and V to Regulation (EC) No 396/2005 of the European Parliament and of the Council as Regards Maximum Residue Levels for Ametoctradin, Chlorothalonil, Diphenylamine, Flonicamid, Fluazinam, Fluoxastrobin, Halauxifen-Methyl, Propamocarb, Prothioconazole, Thiacloprid and Trifloxystrobin in or on Certain Products (Text with EEA Relevance). Available online: http://data.europa.eu/eli/reg/2016/67/oj (accessed on 10 August 2026).
82. Qin, Y.; Zhang, Y.; Chen, Y.; Lin, S.; Shu, Y.; Huang, Y.; Huang, X.; Zhou, M. Impact of Snow on Underground Smoldering Wildfire in Arctic-Boreal Peatlands. *Environ. Sci. Technol.* **2025**, *59*, 3915–3924. [CrossRef] [PubMed]
83. ImageJ: Image Processing and Analysis in Java. Available online: https://imagej.net/ij/ (accessed on 1 April 2025).
84. Zhou, G.-T.; Yu, J.C.; Wang, X.-C.; Zhang, L.-Z. Sonochemical synthesis of aragonite-type calcium carbonate with different morphologies. *New J. Chem.* **2004**, *28*, 1027–1031. [CrossRef]
85. Sahadat Hossain, M.; Ahmed, S. Crystallographic characterization of naturally occurring aragonite and calcite phase: Rietveld refinement. *J. Saudi Chem. Soc.* **2023**, *27*, 101649. [CrossRef]
86. Baumgartner, J.; Arita-Merino, N.; Schwager, N.; Spahn, D.; Ambrosioni, M.; Thaler, S.; Radiom, M.; Boulos, S.; Dumpler, J.; Fischer, P.; et al. The potential of lipid droplets from the microalga Chlamydomonas reinhardtii as natural emulsions. *Food Hydrocoll.* **2026**, *172*, 112114. [CrossRef]
87. Hossain, M.; Muntaha, N.; Osman Goni, L.K.M.; Jamal, M.S.; Gafur, M.A.; Islam, D.; Fakhruddin, A.N.M. Triglyceride Conversion of Waste Frying Oil up to 98.46% Using Low Concentration K+/CaO Catalysts Derived from Eggshells. *ACS Omega* **2021**, *6*, 35679–35691. [CrossRef] [PubMed]
88. Scolari, S.; Mombelli, D.; Dall'Osto, G.; Mapelli, C. Effect of water-powder interaction on the mechanical and metallurgical behavior of integrated steel plant byproducts agglomerates. *Particuology* **2025**, *105*, 74–87. [CrossRef]
89. Zhao, J.; Liu, H.; Li, X. Structure, Property, and Performance of Catalyst Layers in Proton Exchange Membrane Fuel Cells. *Electrochem. Energy Rev.* **2023**, *6*, 13. [CrossRef] [PubMed]
90. Wanwimolruk, S.; Phopin, K.; Boonpangrak, S.; Prachayasittikul, V. Food safety in Thailand 4: Comparison of pesticide residues found in three commonly consumed vegetables purchased from local markets and supermarkets in Thailand. *PeerJ* **2016**, *4*, e2432. [CrossRef] [PubMed]
91. Thummajitsakul, S.; Subsinsungnern, R.; Treerassapanich, N.; Kunsanprasit, N.; Puttirat, L.; Kroeksakul, P.; Silprasit, K. Pesticide and heavy metal contamination: Potential health risks of some vegetables and fruits from a local market and family farm in Ongkharak District of Nakhon Nayok Province, Thailand. *Pertanika J. Trop. Agric. Sci.* **2018**, *41*, 987–1001.
92. *EN 15662:2018*; Foods of Plant Origin—Multimethod for the Determination of Pesticide Residues Using GC- and LC-Based Analysis Following Acetonitrile Extraction/Partitioning and Clean-Up by Dispersive SPE—Modular QuEChERS-Method. European Committee for Standardization (CEN): Brussels, Belgium, 2018.
93. Arserim-Uçar, D.K.; Korel, F.; Liu, L.; Yam, K.L. Characterization of bacterial cellulose nanocrystals: Effect of acid treatments and neutralization. *Food Chem.* **2021**, *336*, 127597. [CrossRef] [PubMed]
94. Silva, J.M.; Barud, H.S.; Meneguin, A.B.; Constantino, V.R.L.; Ribeiro, S.J.L. Inorganic-organic bio-nanocomposite films based on Laponite and Cellulose Nanofibers (CNF). *Appl. Clay Sci.* **2019**, *168*, 428–435. [CrossRef]
95. Lertwattanaruk, P.; Makul, N.; Siripattarapravat, C. Utilization of ground waste seashells in cement mortars for masonry and plastering. *J. Environ. Manag.* **2012**, *111*, 133–141. [CrossRef] [PubMed]
96. Lertvachirapaiboon, C.; Pienpinijtham, P.; Wongravee, K.; Ekgasit, S. Optical Properties of Individual Aragonite Plates from Nacre. *ChemistrySelect* **2018**, *3*, 11700–11704. [CrossRef]
97. Kontoyannis, C.G.; Vagenas, N.V. Calcium carbonate phase analysis using XRD and FT-Raman spectroscopy. *Analyst* **2000**, *125*, 251–255. [CrossRef]
98. Ismail, R.; Cionita, T.; Shing, W.L.; Fitriyana, D.F.; Siregar, J.P.; Bayuseno, A.P.; Nugraha, F.W.; Muhamadin, R.C.; Junid, R.; Endot, N.A. Synthesis and Characterization of Calcium Carbonate Obtained from Green Mussel and Crab Shells as a Biomaterials Candidate. *Materials* **2022**, *15*, 5712. [CrossRef] [PubMed]

99. Xu, S.; Cai, S.; Huang, R.; Fu, D.; Fang, L.; Zhang, C.; Ma, Z. Novel Sustainable Pavement Material: Recycling of Waste Shells as the Filler of Asphalt Mastic. *ACS Sustain. Chem. Eng.* **2024**, *12*, 13048–13061. [CrossRef]
100. Zare, M.; Figueiredo, P.C.; Lahtinen, M.H.; Hilden, K.S.; Hietala, S.; Mikkonen, K.S. Interfacial Properties of Surface-Modified Lignin Nanoparticles. *Langmuir* **2025**, *41*, 17654–17667. [CrossRef] [PubMed]
101. Sakr, H.; Ammar, A.; Zaki, H.; Salama, M.A.; Ali, M. Impact of ball milling on physicochemical, structural, and functional properties of Moringa oleifera L. leaf powders. *J. Food Meas. Charact.* **2024**, *18*, 320–330. [CrossRef]
102. Seepma, S.Y.M.H.; Ruiz-Hernandez, S.E.; Nehrke, G.; Soetaert, K.; Philipse, A.P.; Kuipers, B.W.M.; Wolthers, M. Controlling $CaCO_3$ Particle Size with $\{Ca^{2+}\}$:$\{CO_3^{2-}\}$ Ratios in Aqueous Environments. *Cryst. Growth Des.* **2021**, *21*, 1576–1590. [CrossRef] [PubMed]
103. Claesson, P.M.; Wojas, N.A.; Corkery, R.; Dedinaite, A.; Schoelkopf, J.; Tyrode, E. The dynamic nature of natural and fatty acid modified calcite surfaces. *Phys. Chem. Chem. Phys.* **2024**, *26*, 2780–2805. [CrossRef] [PubMed]
104. Tsuboi, M.; Tamura, K.; Kitanaka, R.; Oka, H.; Akao, K.-I.; Ozaki, Y. Attenuated Total Reflection Infrared and Far-Infrared, and Raman Spectroscopy Studies of Minerals, Rocks, and Biogenic Minerals. *Appl. Spectrosc.* **2024**, *78*, 186–196. [CrossRef] [PubMed]
105. Abdelmageed, G.; Kahwagi, R.F.; Korkomaz, J.; El-Halaby, A.; Leontowich, A.F.G.; Hinds, S.; Koleilat, G.I. The efficacy of oleic acid treatment in passivating MAPbI3 films. *Nanoscale* **2025**, *17*, 11646–11657. [CrossRef] [PubMed]
106. Kuang, J.; Wang, X.; Yu, M.; Yuan, W.; Huang, Z.; Zhang, S.; Xiao, J. Flotation behavior and mechanism of calcium carbonate polymorphs with sodium oleate as collector. *Powder Technol.* **2022**, *398*, 117040. [CrossRef]
107. Shi, X.; Rosa, R.; Lazzeri, A. On the Coating of Precipitated Calcium Carbonate with Stearic Acid in Aqueous Medium. *Langmuir* **2010**, *26*, 8474–8482. [CrossRef] [PubMed]
108. Astuto, V.B.; Fernandes, R.; Itri, R.; Petri, D.F.S. Structure–Property Relationship in Cationic Surfactant/Hydroxypropyl Methylcellulose Hydrogels and Cryogels: Role of Headgroup and Counterion Dissociation. *ACS Omega* **2025**, *10*, 56120–56129. [CrossRef] [PubMed]
109. Jaiban, P.; Kongchana, P.; Injay, B.; In-on, N.; Arunroj, P.; Homket, P.; Watcharapasorn, A. The effects of ITO coating on biofilm from durian peel for triboelectric generator. *Chem. Phys. Lett.* **2025**, *869*, 142039. [CrossRef]
110. Ellerbrock, R.H.; Gerke, H.H. FTIR spectral band shifts explained by OM–cation interactions. *J. Plant Nutr. Soil Sci.* **2021**, *184*, 388–397. [CrossRef]
111. Krishna, D.N.G.; Philip, J. Review on surface-characterization applications of X-ray photoelectron spectroscopy (XPS): Recent developments and challenges. *Appl. Surf. Sci. Adv.* **2022**, *12*, 100332. [CrossRef]
112. Wojas, N.A.; Tyrode, E.; Corkery, R.; Ernstsson, M.; Wallqvist, V.; Järn, M.; Swerin, A.; Schoelkopf, J.; Gane, P.A.C.; Claesson, P.M. Calcite Surfaces Modified with Carboxylic Acids (C2 to C18): Layer Organization, Wettability, Stability, and Molecular Structural Properties. *Langmuir* **2023**, *39*, 14840–14852. [CrossRef] [PubMed]
113. Balakrishnan, R.; Dixit, A.; Rao, M.S.R.; Naik, R. Influence of Ca doping on X-ray photoelectron core-level spectra of magnetoelectric bulk $BiFeO_3$. *Surf. Interface Anal.* **2021**, *53*, 798–807. [CrossRef]
114. Ni, M.; Ratner, B.D. Differentiating calcium carbonate polymorphs by surface analysis techniques—An XPS and TOF-SIMS study. *Surf. Interface Anal.* **2008**, *40*, 1356–1361. [CrossRef] [PubMed]
115. Verma, R.; Dabodiya, T.S.; Kumar, A.; Pandey, S.; Jaikumar, T.; Jhaa, G.; Mahishi, A.; Prasath, R.A.; Palantavida, S. Integrated Experimental and DFT Investigations of a Bivalvia Shell Waste-Derived Microcomposite for Sustainable Congo Red Dye Removal via Adsorption and Dye-Sensitized Photocatalysis. *ACS Sustain. Resour. Manag.* **2026**, *3*, 335–348. [CrossRef]
116. Zhang, H.; Sun, W.; Lin, S.; Li, C.; Zhu, Y.; Zhang, C. Mechanistic study on the depression of calcite by sodium hexametaphosphate in sodium oleate system. *Appl. Surf. Sci. Adv.* **2023**, *17*, 100451. [CrossRef]
117. Liu, R.; Huang, S.; Zhang, X.; Song, Y.; He, G.; Wang, Z.; Lian, B. Bio-mineralisation, characterization, and stability of calcium carbonate containing organic matter. *RSC Adv.* **2021**, *11*, 14415–14425. [CrossRef] [PubMed]
118. Guo, W.; Zhang, H.; Lu, H.; Zhang, Z.; Liu, D.; Wu, H. Elucidating the Mechanism and Performance of Sodium Oleate Direct Flotation for Hemimorphite: A Novel Hallimond Tube Approach. *ACS Omega* **2025**, *10*, 44499–44509. [CrossRef] [PubMed]
119. Wen, Y.; Qing, H.; Shu, H.; Liu, Q. Evaluating the Protective Effects of Calcium Carbonate Coating on Sandstone Cultural Heritage. *Coatings* **2021**, *11*, 1534. [CrossRef]
120. Wang, Y.; Jiang, S.; Chen, Y.; Qiu, D.; Weng, Y. Synthesis and Characterization of a Novel Composite Edible Film Based on Hydroxypropyl Methyl Cellulose Grafted with Gelatin. *Gels* **2023**, *9*, 332. [CrossRef] [PubMed]
121. Ye, Y.; Zhang, L.; Zhu, Z.; Xie, F.; Meng, L.; Yang, T.; Qian, J.-Y.; Chen, Y. Facile superhydrophobic modification on HPMC film using polydimethylsiloxane and starch granule coatings. *Int. J. Biol. Macromol.* **2024**, *266*, 131191. [CrossRef] [PubMed]
122. Chiaregato, C.G.; Bernardinelli, O.D.; Shavandi, A.; Sabadini, E.; Petri, D.F.S. The effect of the molecular structure of hydroxypropyl methylcellulose on the states of water, wettability, and swelling properties of cryogels prepared with and without CaO_2. *Carbohydr. Polym.* **2023**, *316*, 121029. [CrossRef] [PubMed]
123. Malik, G.K.; Khuntia, A.; Mitra, J. Comparative Effect of Different Plasticizers on Barrier, Mechanical, Optical, and Sorption Properties of Hydroxypropyl Methylcellulose (HPMC)–Based Edible Film. *J. Biosyst. Eng.* **2022**, *47*, 93–105. [CrossRef]

124. Lee, S.; Kim, E.; Lee, D.; Jang, K.; Park, J.; Choi, W.Y. Synthesis of seawater-derived superhydrophobic calcium carbonate via CO_2 mineralization by utilizing L-Arginine/L-Lysine oleate-based self-assembly structures. *Chem. Eng. J.* **2024**, *490*, 151785. [CrossRef]
125. Bilbao-Sáinz, C.; Avena-Bustillos, R.J.; Wood, D.F.; Williams, T.G.; McHugh, T.H. Composite Edible Films Based on Hydroxypropyl Methylcellulose Reinforced with Microcrystalline Cellulose Nanoparticles. *J. Agric. Food Chem.* **2010**, *58*, 3753–3760. [CrossRef] [PubMed]
126. Li, Z.; Ma, X.; Kong, Q.; Zang, D.; Guan, X.; Ren, X. Static and Dynamic Hydrophobic Properties of Honeycomb Structured Films via Breath Figure Method. *J. Phys. Chem. C* **2016**, *120*, 18659–18664. [CrossRef]
127. Xiong, B.; Li, J.; He, C.; Tang, X.; Lv, Z.; Li, X.; Yan, X. Effect of pore morphology and surface roughness on wettability of porous titania films. *Mater. Res. Express* **2020**, *7*, 115013. [CrossRef]
128. Guo, X.; Li, X.; Chan, L.; Huang, W.; Chen, T. Edible $CaCO_3$ nanoparticles stabilized Pickering emulsion as calcium-fortified formulation. *J. Nanobiotechnol.* **2021**, *19*, 67. [CrossRef] [PubMed]
129. Rosenbloom, R.A.; Zhao, Y. Hydroxypropyl methylcellulose or soy protein isolate-based edible, water-soluble, and antioxidant films for safflower oil packaging. *J. Food Sci.* **2021**, *86*, 129–139. [CrossRef] [PubMed]
130. Yang, Y.; Mao, L.; Zhu, Y.; Yu, J.; Luo, Z.; Lin, X. The spatial distribution and migration of three typical fungicides in postharvest satsuma mandarin (*Citrus unshiu* Marc.) fruit. *Food Sci. Technol. Int.* **2023**, *29*, 510–517. [CrossRef] [PubMed]
131. Hrynko, I.; Kaczyński, P.; Pietruszyńska, M.; Łozowicka, B. The effect of food thermal processes on the residue concentration of systemic and non-systemic pesticides in apples. *Food Control* **2023**, *143*, 109267. [CrossRef]
132. Gao, W.; Du, X.; Gao, Z.; Dai, H.; Li, L.; Zhang, B.; Wang, G.; Chen, X.; Doherty, J.; Clark, J.M.; et al. Assessing the effect of a non-ionic surfactant on surface degradation of the pesticide Acetamiprid on live tea plants. *Food Res. Int.* **2025**, *221*, 117341. [CrossRef] [PubMed]
133. Du, J.; Zhu, Q.; Guo, J.; Gu, J.; Guo, J.; Wu, Y.; Ren, L.; Yang, S.; Jiang, J. Preparation and characterization of edible films from gelatin and hydroxypropyl methyl cellulose/sodium carboxymethyl cellulose. *Heliyon* **2025**, *11*, e41613. [CrossRef] [PubMed]
134. Pirzada, T.; Sohail, M.; Tripathi, A.; Farias, B.V.; Mathew, R.; Li, C.; Opperman, C.H.; Khan, S.A. Toward Sustainable Crop Protection: Aqueous Dispersions of Biodegradable Particles with Tunable Release and Rainfastness. *Adv. Funct. Mater.* **2022**, *32*, 2108046. [CrossRef]
135. Shanbhag, C.; Shenoy, R.; Shetty, P.; Srinivasulu, M.; Nayak, R. Formulation and characterization of starch-based novel biodegradable edible films for food packaging. *J. Food Sci. Technol.* **2023**, *60*, 2858–2867. [CrossRef] [PubMed]
136. Mallmann, G.C.; Tomazelli, D.; Camargo, L.S.; da Cruz, S.P.; de Oliveira Filho, L.C.I.; Sousa, J.P.; Klauberg-Filho, O. Risk assessment of fungicides on symbiotic phase of arbuscular mycorrhizal fungi. *Ecotoxicology* **2026**, *35*, 75. [CrossRef] [PubMed]
137. Wang, H.; Xu, C.; Wen, A.; Du, Y.; Yuan, S.; Yu, H.; Guo, Y.; Cheng, Y.; Qian, H.; Yao, W. The adsorption-desorption behavior of chlorothalonil in the cuticles of apple and red jujube. *Sci. Total Environ.* **2024**, *935*, 173195. [CrossRef] [PubMed]

Disclaimer/Publisher's Note: The statements, opinions and data contained in all publications are solely those of the individual author(s) and contributor(s) and not of MDPI and/or the editor(s). MDPI and/or the editor(s) disclaim responsibility for any injury to people or property resulting from any ideas, methods, instructions or products referred to in the content.